Title
Optical Orientation of Nuclear Spins

Author
King, Jonathan Patrick

Publication Date
2012

Peer reviewed|Thesis/dissertation

Optical Orientation of Nuclear Spins

by

Jonathan King

A dissertation submitted in partial satisfaction of the
requirements for the degree of
Doctor of Philosophy

in

Chemical Engineering

in the

Graduate Division

of the

University of California, Berkeley

Committee in charge:

Professor Jeffrey A. Reimer, Chair
Professor Dmitry Budker
Professor David Graves

Fall 2012

Optical Orientation of Nuclear Spins

Abstract

Optical Orientation of Nuclear Spins

by

Jonathan King

Doctor of Philosophy in Chemical Engineering

University of California, Berkeley

Professor Jeffrey A. Reimer, Chair

Nuclear spins are harnessed in many important technologies, including the well established fields of magnetic resonance imaging for medical diagnostics, magnetic resonance spectroscopy in analytical chemistry as well as emerging technologies in quantum information and spintronics. All of these technologies either harness, or are subject to, the behavior of a nuclear spin ensemble. To achieve the most desirable behavior, (large spectroscopic signal or reduction of unwanted fluctuations) the nuclear spin ensemble should be prepared in a pure quantum state. In practice, this "polarization" is typically created by allowing the energy levels of the spins in an applied magnetic field achieve thermal equilibrium. Unfortunately, even with the largest magnets available with fields greater than 20 Tesla, the separation between energy levels is much smaller than kT for all but extreme refrigerated systems. It is then desirable to achieve pure nuclear spin states which are not at thermal equilibrium with the environment. In order to do this, it is necessary to create a situation in which a pure quantum state can be created in a system other than the nuclear spin which then interacts with the nucleus to create a more pure nuclear spin state. In this work we harness the pure photon spin state of circularly polarized light as well as spin transition selection rules of a deep electronic defect in diamond to polarize nuclei.

In the first case, we use circularly polarized photons to excite spin polarized electrons in the semiconductor gallium arsenide which equilibrate with bound electronic states at recombination centers. These bound states then polarize nearby nuclear spins through the magnetic hyperfine interaction. While this hyperfine mechanism of nuclear spin polarization was previously known, we have identified a new regime of low optical absorption where the coupling of nuclear quadrupole moments to electric field gradients near recombination centers is the dominant mechanism of nuclear spin polarization. Through a combination of experiment and theory, we determine relative rates of these two mechanisms depending on the rate of optical absorption. Since optical absorption varies as a function of depth in a sample, we predicted that control of these two mechanisms is possible as a function of position in the sample. Using the stray field of a superconducting magnet to supply the gradient field for magnetic resonance imaging, we were able to directly observe patterns of

nuclear magnetization on a micron length scale. When combined with in-plane control of the laser and NMR pulse sequences, this technique will give rise to fully 3-dimensional patterns of nuclear magnetization. These patterns may be created in bulk gallium arsenide without the need for lithography or other microfabrication techniques. These regions of magnetized nuclei will enable magnetic control over drifting electrons in future spintronics devices.

The paramagnetic nitrogen-vacancy defect in diamond provides a different tool to control nuclei. The ground state spin triplet of this defect may be easily polarized into the $S_z = 0$ state with visible optical illumination. The polarization is due to the symmetry and selection rules within the defect itself and does not require polarized photons. We discovered that, with a sufficient density of defects, the ^{13}C nuclei in the diamond lattice are spontaneously polarized upon illumination of the sample. We attribute this polarization to a highly refrigerated "spin temperature" among the energy levels created by the magnetic dipole interaction of the many spins in the defect ensemble. This energy reservoir is in thermal contact with the ^{13}C nuclei, which are driven to highly athermal spin states. We theoretically investigate the thermodynamics of the defect spin ensemble, first with a two-spin "toy model" and more recently have begun a many-spin theoretical approach. The polarization of nuclei in diamond has application in the quenching of nuclear fluctuations in quantum information systems and as a platform for signal enhancement in magnetic resonance imaging and spectroscopy.

To Mom, Dad, and Sara

Contents

List of Figures

List of Tables

Acknowledgments

In dealing with his students, Jeff Reimer's priorities lie in this order: the student's personal well being, the student's academic success, and only then comes his own professional success. Anyone who works in academia will recognize how rare this quality is and how lucky his students are to have such a mentor. Jeff's limitless patience and optimism carried me through the early days of my project when I felt lost and directionless and his trust and willingness to grant me freedom let me reach my potential once I felt ready to start taking command of my path through science.

The Reimer lab is a special place that seems to attract a unique brand of researcher, many of whom have enriched my personal and professional lives. I began my career under the mentorship of Pat Coles. From Pat I learned the value of intellectual rigor and that you never have to compromise in the search to understand. I leave knowing that the optical pumping project in the Reimer is in good hands. Eric Scott is an experimental master and Melanie Drake is well down the path to understanding the mysteries of diamond.

I am always impressed by the generosity of fellow scientists. Carlos Meriles and Yunpu Li supplied their experimental expertise and let me take the lead as a theorist in my most fruitful collaboration. Dima Budker provided me with a diamond when when we lost ours.

My first science lessons came from my father and I have never wanted to stop learning. My mother, the artist, helped me realize my intuition, and that you can often see the answer even before you can prove it. My parents let me become who I wanted to be and make my own path through life.

I have made many friends in Berkeley, but I especially need to acknowledge my roommates from the Addison House. Victor is the best person I know to sit around and do nothing with, Eddy is my best climbing partner, and Ben keeps us all in line. Last, but certainly not least, Sara's companionship and unconditional support keep me optimistic when all else fails.

Chapter 1

Introduction

1.1 Spin Magnetic Resonance

The subject of magnetic resonance has been covered in great detail in many excellent texts (such as those by Abragam and Slichter); here I will give only a brief introduction to the subject of high-field, pulsed magnetic resonance. Magnetic resonance spectroscopy is the experimental interrogation of the magnetic transitions of particles that possess magnetic dipole moments (which are aligned with the spin angular momentum of the particle). In the high-field regime encountered in this work, the dominant term in the Hamiltonian (called the Zeeman interaction) is the result of a static, external magnetic field applied by the experimental apparatus. The spectroscopically interesting features of the system under study then reveal themselves as small perturbations to the Zeeman Hamiltonian.

A pulsed magnetic resonance experiment generally takes the following steps. First, the populations of the energy levels (as determined by the Zeeman Hamiltonian) are allowed to come to thermal equilibrium, creating some degree of spin order. Next, a pulsed, oscillating magnetic field is applied perpendicular to the Zeeman field at the nuclear Larmor frequency. The pulse is timed to convert the Zeeman spin order in to a coherent superposition of Zeeman states. This ensemble superposition state then interacts with the inductive detection coil to coherently emit and absorb photons (to the coil, not the radiation field!) in an oscillatory fashion. This oscillation at the Larmor frequency is recorded as an induced voltage in the detection coil, yielding the magnetic resonance signal. A Fourier transform of the oscillating signal yields the familiar spectrum representation of the magnetic resonance signal. The internal spin Hamiltonian of the sample yields many subtle perturbations to the observed signal, which are responsible for widespread application of NMR as an analytical technique. In this work, it is important to understand that magnitude of the observed signal is directly related to the initial (typically very small) spin order. It is this initial order (or polarization, or magnetization) that we seek to enhance and control.

1.2 Spin Thermodynamics

The Density Operator Description

Because this work exclusively deals with large ensembles of spins, it is usually convenient to use the density operator description of quantum mechanics. The density operator (ρ) is simply defined as the outer product of a quantum mechanical state vector with its adjoint, or conjugate transpose:

$$\rho = |\Psi >< \Psi| \tag{1.1}$$

Schrödinger's equation is then rearranged to form the Liouville equation for the time evolution of the density operator:

$$\frac{\partial \rho}{\partial t} = \frac{1}{i\hbar}[H, \rho]. \tag{1.2}$$

So far this is rigorously equivalent to the state vector description of quantum mechanics. If we have a system of N identical spins that are weakly coupled, it is often a good approximation to represent the state of the system as a single density operator which is the sum of many single-spin operators:

$$\rho_{ensemble} = \frac{1}{N}\sum_{i=1}^{N} \rho_i. \tag{1.3}$$

This approximation reduces the state of the system from an operator on a $(2I+1)^N$-dimensional vector space to a $(2I+1)$-dimensional space. In exchange for this simplification, coherences (superposition states) involving more than one spin are not represented and their effects appear as non-unitary evolution of the density operator along with spin-environment interactions. The main advantage of this representation is that the ensemble density operator represents both the statistical and quantum mechanical nature of the system. For example, the ensemble average of a quantity represented by an observable operator O is:

$$< O >= \text{trace}(\rho O). \tag{1.4}$$

Often we will be concerned with the total energy in the spin system, which is:

$$E =< H >= \text{trace}(\rho H). \tag{1.5}$$

We can also define the density operator at thermal equilibrium:

$$\rho(T) = \frac{e^{-H/kT}}{\text{trace}(e^{-H/kT})}. \tag{1.6}$$

The exponential of an operator, which is itself typically represented as a matrix, can cause some confusion in this equation. This is easily resolved by representing the exponential as a Taylor series:

$$e^{-H/kT} =\sim I - \frac{H}{kT} + \frac{H^2}{2(kT)^2} - \frac{H^3}{6(kT)^3}... \tag{1.7}$$

where the usual rules for matrix multiplication apply so that the result is also an operator on the same vector space as H.

These expressions are especially powerful because the trace is invariant under similarity transformations, meaning one can represent the observable operators and density operator in any basis set that is convenient. This is especially useful when studying the angular dependence of spin phenomena. If we work in a basis where the Hamitonian is diagonal, the equilibrium density operator will also be diagonal, with the diagonal elements equal to the population of each corresponding energy level as expected for Boltzmann statistics.

The Problem of Polarization

Most magnetic resonance spectroscopy and imaging techniques involve the observation of bulk magnetization. The operator for magnetization is:

$$\bar{\mu} = \frac{g\mu_N}{\hbar}\bar{S} \tag{1.8}$$

where g is the nuclear g-factor, μ_N is the nuclear magneton and $\bar{S}$ is the nuclear spin vector operator. If we measure the z-component of the average nuclear magnetization we obtain:

$$< \mu_z >= \frac{g\mu_N}{\hbar}\,\mathrm{trace}(\rho S_z) \tag{1.9}$$

Since kT is typically very large relative to the eigenvalues of the spin Hamiltonian the density matrix can approximated as a truncated Taylor series:

$$\rho(T) = \frac{e^{-H/kT}}{\mathrm{trace}(e^{-H/kT})} \sim I - \frac{H}{kT} \tag{1.10}$$

where I is the identity operator. Now we evaluate the nuclear magnetization

$$< \mu_z >= \frac{g\mu_N}{\hbar}\,\mathrm{trace}(\rho S_z) = \frac{g\mu_N}{\hbar}\,\mathrm{trace}(S_z - \frac{S_z H}{kT}) = \frac{g\mu_N}{\hbar}\,\mathrm{trace}(\frac{-S_z H}{kT}) \tag{1.11}$$

The final equality results from the fact that spin operators are traceless, leaving only a small term of order $\Delta E/kT$, where ΔE is the separation between eigenvalues of the Hamiltonian. This result is interpreted physically by recognizing that at high temperatures, the density operator is nearly identical to the identity operator which has no contribution to observable magnetization. It is only by introducing order, corresponding to a smaller spin temperature, that the ensemble properties may be harnessed.

Chapter 2

Optical Nuclear Polarization in Diamond

2.1 Introduction

The Nitrogen Vacancy Center in Diamond

The nitrogen vacancy color center in diamond has been the subject of many studies in the last decade. Most studies have focused on quantum control and the use of NV- centers as qubits for quantum information [10, 12, 13, 5, 7, 14, 29], while others have focused on applications such as high-resolution magnetometry[3, 23]. Some of the desirable properties of the nitrogen vacancy center for these applications include: a ground state spin-triplet ($S = 1$), efficient polarization of the ground state triplet into $S_z = 0$ by irradiation in a broad phonon sideband, long spin coherence times, and single-photon emission.

The NV- center, whose structure is shown in figure 2.1, is a negatively charged defect that consists of a substitutional nitrogen adjacent to a vacancy in the diamond lattice. The defect can be modeled as 6 electrons (5 from dangling bonds and one donated from another defect such as the P1 center) or as a 2-hole system with $C3_v$ symmetry. The ground state is a ($^3A_2$) triplet with a spin-spin interaction that splits the $S_Z = 0$ state from the $S_Z = 1$ and $S_Z = -1$ states by 2.88 GHz. The lowest excited state (^3E) is also a triplet with a 1.42 GHz spin-spin interaction. After spin-conserving optical excitation the defect may either decay radiatively into the ground state (also spin-conserving) or undergo intersystem crossing into an ^1E singlet state (this is most likely for the $S_z = +1$ and $S_z = -1$ levels of the excited state triplet.) The intersystem crossings are due to mixing of the singlet and triplet states by weak spin-orbit coupling. The system then decays to the $^1A_1$ singlet state which undergoes another intersystem crossing to preferentially populate the $S_z = 0$ state of the ground state triplet. The spin coherence time of the ground state triplet can be as long as 0.5s, depending on the purity of the diamond[4]. This is due to the largely spin-free carbon lattice (only 1.1% of carbon nuclei have spin). These long-lived, optically initialized spin states in a solid-state system are the basis for quantum information and magnetometry applications.

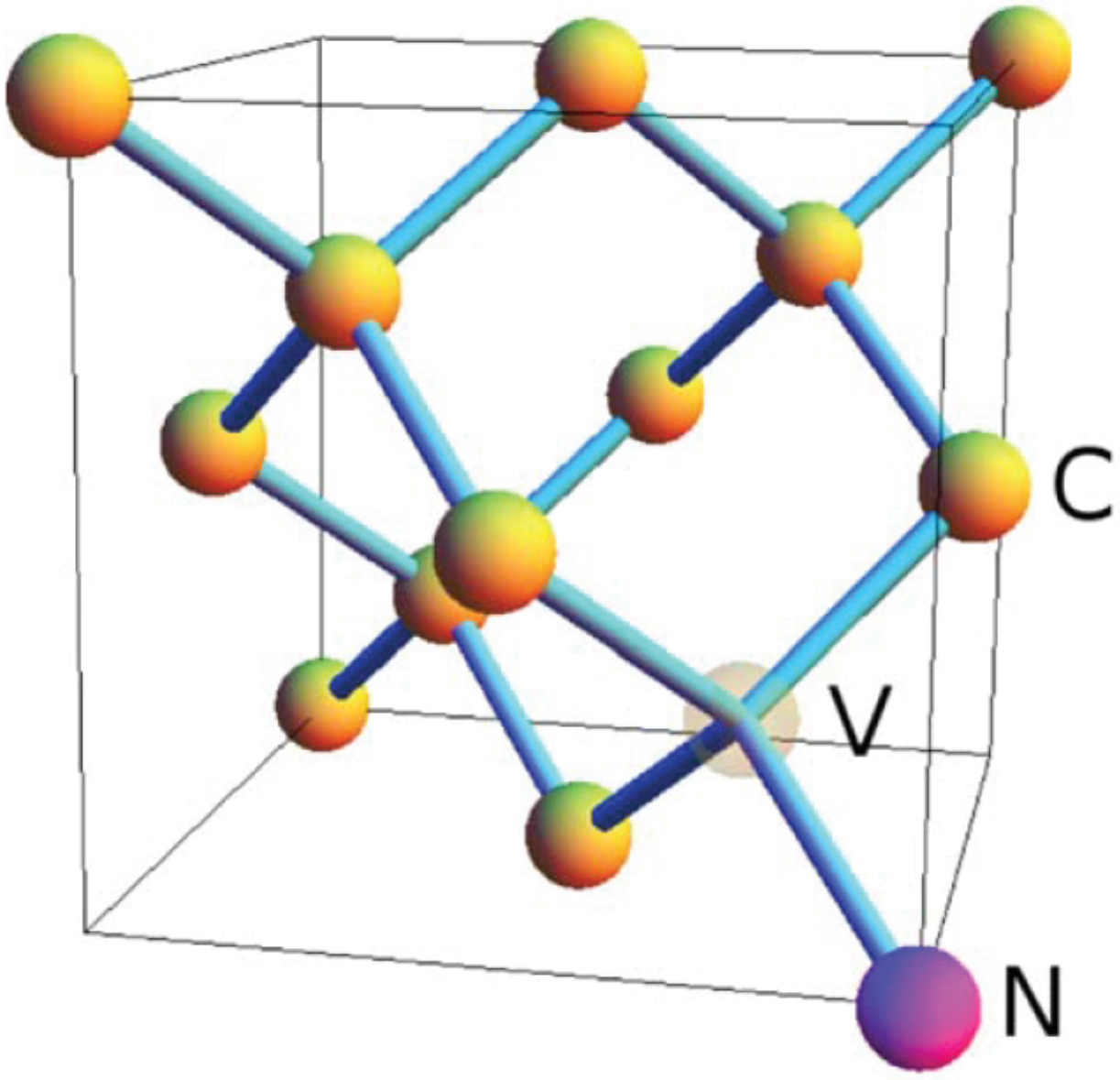

Figure 2.1: Structure of the nitrogen vacancy defect, taken from [2]

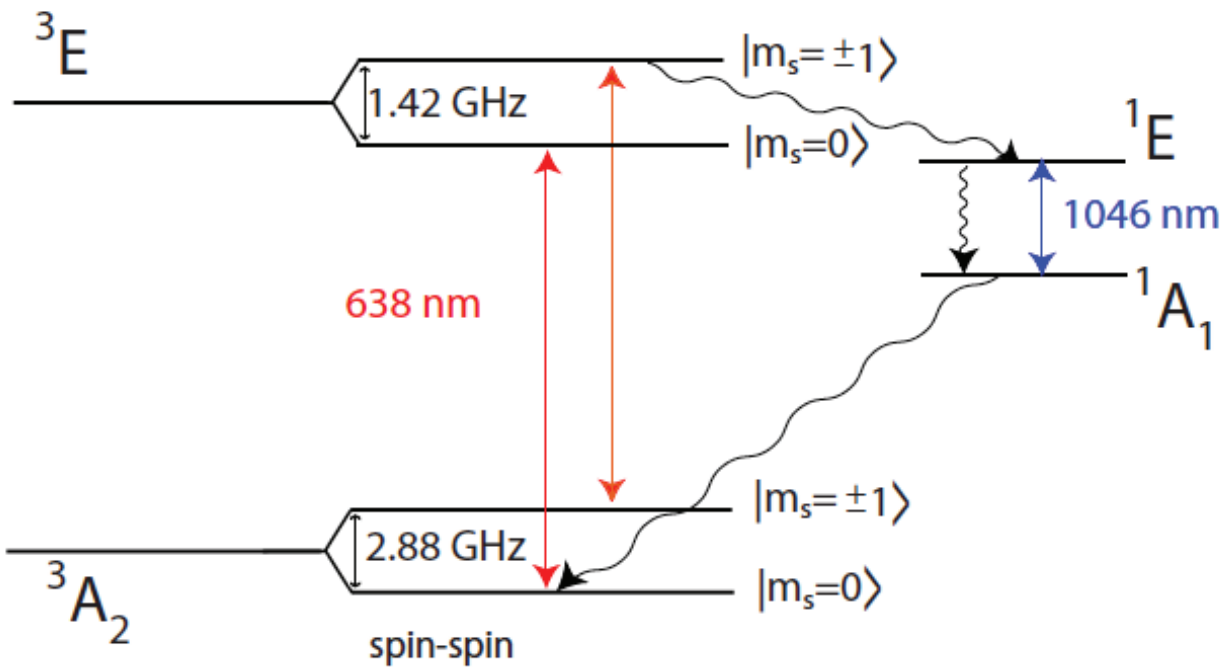

Figure 2.2: Zero-field energy levels of the NV- center showing radiative and non-radiative transitions, taken from [2]

Dynamic Nuclear Polarization in Diamond

Previous work has shown microwave-induced dynamic nuclear nuclear polarization (DNP) of bulk ^{13}C spins in diamond through paramagnetic defects[37],[38],[39]. However, these DNP techniques are limited by the electron Boltzmann factor at the magnetic field strength and temperature used in the experiment. More recently, experiments have shown polarization of the nitrogen nuclear spin of the NV- center, as well as polarization of proximate single ^{13}C spins by making use of the optical polarization of the NV- center[17][13]. However, all of these studies involved polarization and detection of single nuclear spins.

2.2 Experimental

Sample Preparation

The sample used in this study is a high pressure, high temperature (HPHT) synthetic single-crystal diamond purchased from Element-6. Sample dimensions were 3x3x0.5mm with the $< 111 >$ crystal axis aligned along the normal vector to the largest crystal face. One side of the sample is polished. As received, the nitrogen concentration was approximately less than or equal to 200 ppm. The sample was irradiated with 3.0 MeV electrons at a dose of

$\sim 10^{19}\text{cm}^{-2}$, and subsequently annealed at 700, 875 and 1050 degrees Celsius in a forming gas (0.96 atm Ar, 0.04 atm H_2). The final concentration of NV- centers was 8 ppm. Specific details of sample preparation and characterization can be found in [2], where the sample used in this study is labeled as sample 6.

Nuclear Magnetic Resonance

All NMR experiments were carried out in an Oxford 9.4 Tesla superconducting magnet. Spectra were acquired with a Tecmag LapNMR single-resonance spectrometer at 100.59MHz. NMR experiments were carried out using a homebuilt probe employing a flattened split-solenoid coil for optical access. $\frac{\pi}{2}$ pulse lengths for this configuration and the pulse power used were approximately 5.5 microseconds. The sample was mounted to a sapphire plate on the probe which has grooves in which the split solenoid coil resides. Adhesion to the sapphire plate was maintained using a small amount of Apiezon-N grease. The amount of grease used was kept to a minimum in order to avoid background ^{13}C NMR signals. Temperature control was maintained using an Oxford Spectrostat continuous flow helium cryostat with optical access controlled by an Oxford ITC 503 temperature controller. Optical pumping was performed using a Coherent Innova 300 multi-line argon ion laser operating at multiple simultaneous wavelengths ranging from 457.9nm to 514.5nm. Power output from the laser was maintained at 2.5 Watts except for experiments where laser power dependence was studied. Optical pumping experiments were performed by saturation of the ^{13}C spins via a series of RF pulses, followed by an optical pumping delay, then a $\frac{\pi}{2}$ pulse immediately followed by detection of the free-induction decay (FID). Laser irradiation was maintained throughout the entire experiment. Non optically-pumped thermal equilibrium spectra were acquired by cooling the sample to the specified temperature, allowing the spins to equilibrate for a time of two hours, then a $\frac{\pi}{2}$ pulse and detection of the FID. The signal magnitudes in pumped and non-pumped experiments were different such that multiple signal amplifier gains were necessary. In order to correct for the change in receiver gain, signals were calibrated with an external source. Time domain data were Fourier-transformed to obtain a frequency spectrum. A 0^{th} order baseline correction was applied to the frequency spectrum. The integrated area of the NMR peak, proportional to the bulk-averaged nuclear polarization, was calculated. Peak shift and width were obtained by fitting Lorentzian curves to the spectra.

2.3 Results

Polarization Kinetics

Temperature Dependence

Thermal equilibrium NMR spectra were obtained at 50 K. The polarization at equilibrium is given by:

$$P = tanh\left(\frac{\hbar\omega}{k_B T}\right) \tag{2.1}$$

At 50K and $\omega = 2 * \pi * 100.6\text{MHz}$, the polarization P is $\sim *10^{-4}$.
Bulk averaged nuclear polarizations for optically-pumped experiments are obtained by direct ratio of the integral of the NMR peak to the integrated thermal equilibrium peak obtained at 50K, with the necessary normalization for receiver gain and number of scans. Since this is a bulk measurement, it does not provide information about the distribution of polarization within then sample. Figure 2.3 shows the kinetics of the polarization process at temperatures between 5 K and 50 K. Due to the laser powers used in the experiment and the limited cooling capacity of the cryostat near the boiling point of helium, temperature control was poor for experiments at 20 K and lower. This is especially true for the 5 K data, where the measured temperature varied by as much as several K. Additionally, the temperature sensor is not in direct contact with the sample. Therefore we expect that a temperature gradient exists within the cryostat, with the sample at some temperature above the measured temperature. Therefore, the effects of temperature will not be modeled quantitatively, but may be examined as a general trend.

Laser Power Dependence

At a setpoint of 50K, the cooling power of the cryostat was sufficient to maintain stable temperature control. A series of optical pumping experiments using different laser powers was performed at 50K. The results of these experiments are shown in figure 2.4. The magnitude of the polarization increased with increasing laser power. However, the polarization (i.e., the shape of the polarization buildup curve) remained similar.

Temperature Dependence of NMR Lineshape

The NMR lineshape was found to vary with lattice temperature. As shown in table 2.1, at lower temperatures the NMR peak shifted to lower frequencies and broadened significantly. Due to the difficulties of temperature control with high laser power, the temperatures shown are not an accurate measure of lattice temperature, but the trend of the lineshape's dependance on temperature is easily seen.

The shift and with data were extracted by fitting the data with Lorentzian lineshapes. This provided a good fit in all cases while the signal to noise ratio was very high. While it is difficult to extract a meaningful measure of error from these fits, it is clear that the shifts and linewidths are significant.

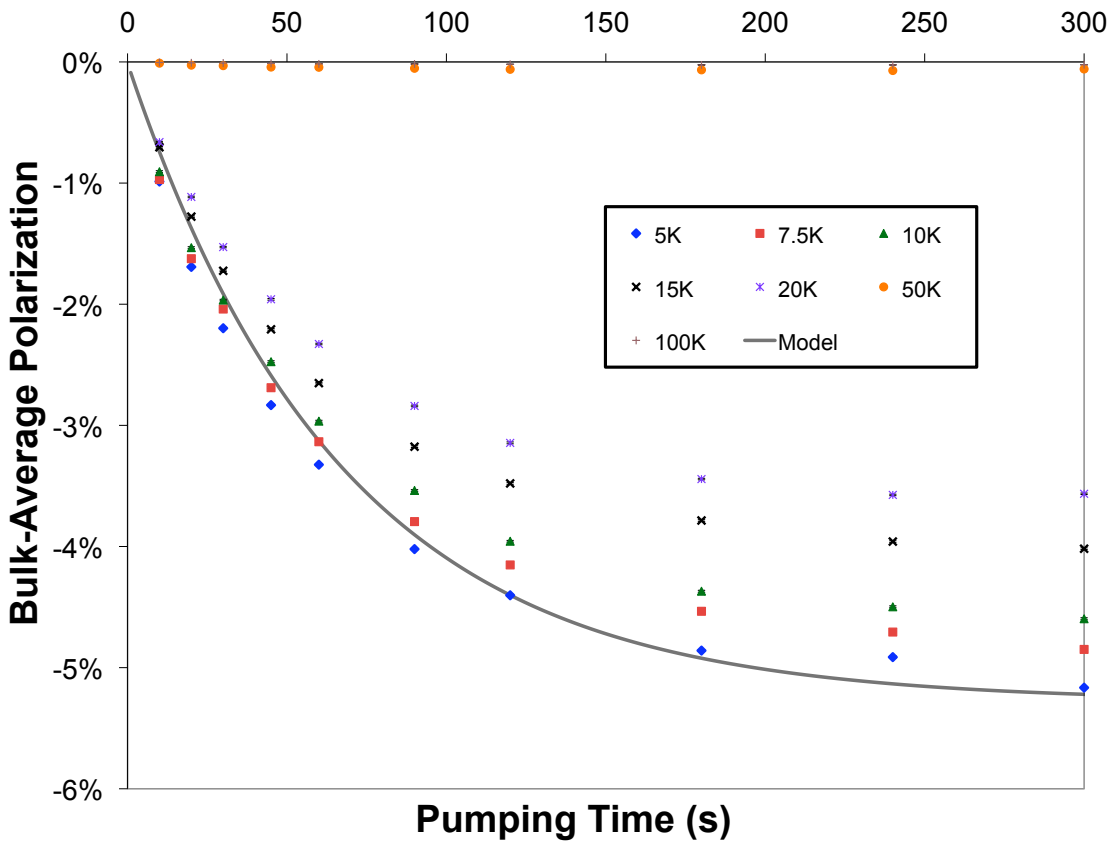

Figure 2.3: ^{13}C polarization kinetics with 2.5W irradiation and varied temperature. The theoretical model is fit to the 5K data. (From [20].)

Temperature	Peak Width	Peak Shift
5K	776Hz	-363Hz
7.5K	757Hz	-315Hz
10K	762Hz	-272Hz
15K	731Hz	-116Hz
20K	698Hz	0Hz

Table 2.1: NMR peak width and shift relative to the peak at 20K, obtained by fitting Lorentzian curves to the data.

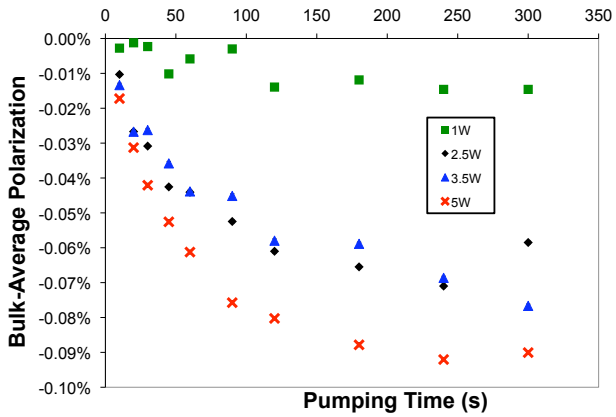

Figure 2.4: Polarization kinetics as a function of laser power at 50K. (From [20].)

2.4 A "Toy Model"

A Thermodynamic View of Spin-Lattice Relaxation

It is well known that high purity diamonds have ^{13}C spin-lattice relaxation times on the order of hours at a field of several Tesla and room temperature, indicating an extremely weak direct coupling between the nuclear spins and lattice phonons[16]. In the case of diamonds containing a large number of paramagnetic impurities, where spin-lattic relaxation times are much shorter, it is valid to consider only the action of the paramagnetic defects in the spin-lattice relaxation mechanism. A thermodynamic description of ^{13}C spin-lattice relaxation in diamonds due to paramagnetic defects has been presented previosly[46]. Following this treatment, we consider the "energy reservoirs" that are assumed to posses internal thermal equilibrium. The important reservoirs are the ^{13}C Zeeman interaction, the paramagnetic defect Zeeman interaction, and the dipole-dipole interaction between paramagnets. The nuclear dipole-dipole interaction is very weak for this dilute spin system and is neglected. The paramagnetic defect-nuclear dipolar interaction is treated as a perturbation that induces transitions as will be shown later, but does not constitute a significant energy reservoir. As shown in figure 2.5, the relaxation of the nuclear Zeeman reservoir can occur directly with the lattice (A), with the electron Zeeman reservoir (B), or with the electron dipole-dipole interaction reservoir (C). Figure 2.5 differentiates between NV- centers and "other" paramagnetic defects, such as substitutional nitrogen and neutral NV centers, in which the electronic spin states are not optically oriented. The arrows represent thermal contact between energy reservoirs.

Relaxation of the nuclear Zeeman energy reservoir for a spin-$\frac{1}{2}$ nucleus is induced by fluctuating magnetic fields at the NMR frequency ($\sim$100MHz). Fluctuations due to spin-lattice relaxation of paramagnetic defects, governed by a relaxation time T_{1e}, give rise to a direct

coupling between the nuclear Zeeman reservoir and lattice phonons ("A" in figure 2.5). It has been shown that at temperatures less than 100K T_{1e} can be several seconds or more, so the spectral density of these fluctuations at the NMR frequency is very small [45, 18]. All other spin-lattice relaxation pathways involve relaxation of paramagnetic Zeeman reservoirs with the lattice (arrows "B"). Again, as these relaxation times become long, the coupling between the nuclei and the lattice becomes weak.

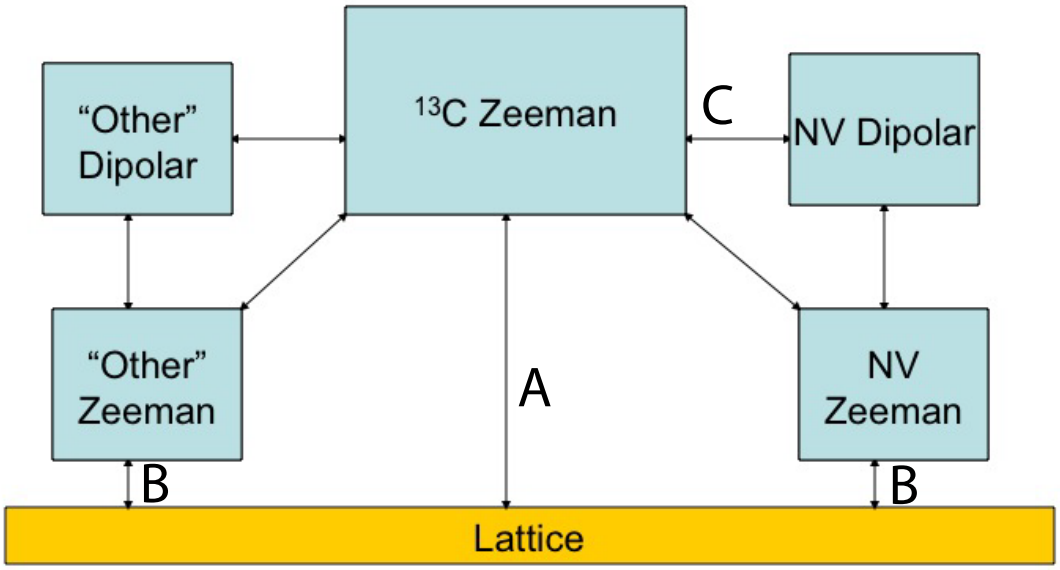

Figure 2.5: Thermodynamic model of spin-lattice relaxation in diamond showing energy reservoirs and relaxation pathways.

Since both the electron and nuclear spins are effectively decoupled from the lattice, we might expect that interaction between the nuclear Zeeman reservoir and optically-pumped NV- centers will result in athermal populations of nuclear spin states. The coupling between the ^{13}C Zeeman system and the NV- center Zeeman reservoir is weak because there is no energy-conserving 2-spin flip flop or 3-spin process that couples these two reservoirs. The

latter statement's validity can be seen by examining the electron spin resonance spectrum, for example [45], and finding no NV- center lines are separated by a frequency equal to the ^{13}C Larmor frequency. It is however possible for a transition among the dipolar energy levels of the NV- centers to be on resonance with the nuclear transition, thereby establishing thermal contact between the ^{13}C Zeeman energy reservoir and the NV- center dipolar energy reservoir (C in figure 2.5).

Energy Level Structure

Spin Hamiltonian

In the thermodynamic context, we are investigating thermal contact between energy reservoirs. In order to continue in this manner, we must determine the effective temperature of the NV- center dipolar energy reservoir, which in turn requires detailed knowledge of the energy level structure of the NV- centers. We consider pairwise dipolar interactions between separate NV- centers for which we determine energy levels and eigenfunctions. The the full spin Hamiltonian is then given by:

$$\mathcal{H} = \mathcal{H}_Z + \mathcal{H}_{DD} + \mathcal{H}_{SS} \tag{2.2}$$

where Z represents the Zeeman interaction, DD represents the electron dipole-dipole interaction between separate defect centers, and SS represents the spin-spin splitting of the NV- center Zeeman levels due to the two electrons contained within a single defect. In the Zeeman basis, the basis vectors are:
$|S_Z^1, S_Z^2>=$
$|1,1>, |1,0>, |0,1>, |-1,1>, |0,0>, |1,-1>, |-1,0>, |0,-1>, |-1,-1>$

The indices 1 and 2 refer to different defect centers. The vector connecting the two defects has a length r, and an angle θ with the z-axis (defined by the external magnetic field). Retaining only those terms which commute with the Zeeman Hamiltonian, the total spin Hamiltonian can then be written in matrix form:

$$\mathcal{H} = \begin{pmatrix} A+2Z+2D & 0 & 0 & 0 & 0 & 0 & 0 & 0 & 0 \\ 0 & Z+D & B & 0 & 0 & 0 & 0 & 0 & 0 \\ 0 & B & Z+D & 0 & 0 & 0 & 0 & 0 & 0 \\ 0 & 0 & 0 & -A+2D & B & 0 & 0 & 0 & 0 \\ 0 & 0 & 0 & B & 0 & B & 0 & 0 & 0 \\ 0 & 0 & 0 & 0 & B & -A+2D & 0 & 0 & 0 \\ 0 & 0 & 0 & 0 & 0 & 0 & -Z+D & B & 0 \\ 0 & 0 & 0 & 0 & 0 & 0 & B & -Z+D & 0 \\ 0 & 0 & 0 & 0 & 0 & 0 & 0 & 0 & A-2Z+2D \end{pmatrix} \tag{2.3}$$

where

$$Z = \hbar\gamma_{NV}B_0 \tag{2.4}$$

$$A = \frac{\mu_0}{4\pi}\hbar\gamma_{NV}^2\frac{1}{r^3}[1 - 3cos^2\theta] \tag{2.5}$$

$$B = -\frac{1}{4}\frac{\mu_0}{4\pi}\hbar\gamma_{NV}^2\frac{1}{r^3}[1 - 3cos^2\theta] \tag{2.6}$$

D is the spin-spin splitting and will be calculated in the next section. This Hamiltonian can now be diagonalized to find the eigenvectors and corresponding energy levels. Using these new eigenvectors $|n>$ as our basis we have:

$$\begin{aligned}
|1> &= \frac{1}{\sqrt{2}}(-|-1,1> + |1,-1>) \\
|2> &= \frac{1}{N_1}(|-1,1> + (\frac{-A + 2\Gamma + \sqrt{A^2 + 8B^2 - 4AD + 4D^2}}{2B})|0,0> + |1,-1>) \\
|3> &= \frac{1}{N_2}(|-1,1> + (\frac{-A + 2\Gamma - \sqrt{A^2 + 8B^2 - 4AD + 4D^2}}{2B})|0,0> + |1,-1>) \\
|4> &= |-1,-1> \\
|5> &= \frac{1}{\sqrt{2}}(-|-1,0> + |0,-1>) \\
|6> &= \frac{1}{\sqrt{2}}(|-1,0> + |0,-1>) \\
|7> &= \frac{1}{\sqrt{2}}(-|1,0> + |0,1>) \\
|8> &= \frac{1}{\sqrt{2}}(|0,1> + |1,0>) \\
|9> &= |1,1>
\end{aligned} \tag{2.7}$$

N_1 and N_2 are normalization factors given by:

$$N_1 = \sqrt{2 + \frac{1}{4}\left(\frac{-A + 2\Gamma + \sqrt{A^2 + 8B^2 - 4AD + 4D^2}}{B}\right)^2} \tag{2.8}$$

$$N_2 = \sqrt{2 + \frac{1}{4}\left(\frac{-A + 2\Gamma - \sqrt{A^2 + 8B^2 - 4AD + 4D^2}}{B}\right)^2} \tag{2.9}$$

Due to the large difference between γ_{NV} and $\gamma_{^{13}C}$, transitions that involve $\Delta S_Z \geq 1$ cannot induce a nuclear Zeeman transition. In order to see how transitions among energy levels can give rise to polarized nuclei, we will confine the analysis to the manifold of states with zero total spin angular momentum, $|1>$, $|2>$, and $|3>$ (Valid if optical pumping into $S_z = 0$ is efficient. Note that other states, if populated, can also induce transitions). The energies for these states are given by:

$$E_1 = -A + 2D \tag{2.10}$$

$$E_2 = \frac{1}{2}(-A - \sqrt{8B^2 + (A - 2D)^2} + 2D) \tag{2.11}$$

$$E_3 = \frac{1}{2}(-A + \sqrt{8B^2 + (A - 2D)^2} + 2D) \tag{2.12}$$

Spin-Spin Interaction

Due to axial symmetry of the NV- center defect, the spin-spin interaction Hamiltonian can be written entirely in terms of $S_{z'}$:

$$\mathcal{H}_{SS} = D_0(S_{z'}^2 - \frac{2}{3}) \tag{2.13}$$

where the z'-axis is defined by the symmetry axis of the defect. In this experiment, a $< 111 >$ axis of the crystal is aligned along the magnetic field such that some of the defects have their symmetry axes aligned with the external field. However, due to the tetrahedral symmetry of the lattice, there are an additional 3 equivalent symmetry axes oriented approximately 109.5 degrees from the external field. In order to transform the Hamiltonian from the crystal reference frame to the laboratory frame (i.e. the frame in which we measure nuclear polarization), we recognize that the spin-spin Hamiltonian transforms under rotations like a rank-2 tensor. The Wigner rotation matrices are a useful notation for representing the rotational properties of such entities. Since we only need to retain the part of the transformed Hamiltonian that commutes with S_z, we only need a single element from the rank-2 rotation matrix, $d^2_{0,0}$. In the laboratory frame, the Hamiltonian is given by:

$$\mathcal{H}_{SS} = d^2_{0,0} D_0(S_z^2 - \frac{2}{3}) \tag{2.14}$$

which evaluates as

$$\mathcal{H}_{SS} = D_0 \frac{1}{2}(3\cos^2\theta - 1)(S_z^2 - \frac{2}{3}) = D(S_z^2 - \frac{2}{3}) \tag{2.15}$$

where $D = D_0 \frac{1}{2}(3\cos^2\theta - 1)$.

Optical Pumping of Energy Levels

The optical pumping of NV- centers whose symmetry axes align with the external magnetic field has been extensively treated in literature for low fields, and it is clear that the $S_Z = 0$ state is populated with high efficiency. Even at high field, the symmetry properties of the defect should not change, and a similar polarization is expected. (The case where the magnetic field is not aligned with the defect axis is more complicated and is not treated in this work.) Ensembles of identical spins are most naturally represented as a density matrix. We shall define ρ_{NV} to be the density matrix of a single NV- center under optical pumping. The optical pumping is not expected to give rise to any coherent superposition states, so the off-diagonal elements of ρ_{NV} are all zero and the diagonal elements are the populations of the single-spin sub levels. Although the single-defect density matrix is convenient to define, we are interested in knowing the populations of the 2-defect eigenstates defined in Eqn. 2.7. In order to find these populations, P_i, we use the formula:

$$P_i =< i|(\rho^1_{NV} \otimes \rho^2_{NV})|i > \tag{2.16}$$

where $\rho^1_{NV} \otimes \rho^2_{NV}$ is the density matrix expanded into the 9-dimensional vector space for pair-wise interactions. The superscripts on the density matricies refer to one of the two separate defects under consideration. In order to achieve a fit in our simulations, we assume defects of all orientations have 99.8% of their population in the $S_z = 0$ state (the actual populations for non-aligned defects is likely quite different, and should be accounted for in future work).

Evaluating equation 2.16 for the 3 eigenstates of the total spin Hamiltonian for which $S_Z = 0$ gives:

$$P_1 = \frac{1}{2}\left(P_{|+1>}P_{|-1>} + P_{|-1>}P_{|+1>}\right) \tag{2.17}$$

$$P_2 = \frac{1}{N_1^2}\left(P_{|+1>}P_{|-1>} + P_{|-1>}P_{|+1>} + \alpha^2 P_{|0>}\right) \tag{2.18}$$

$$P_3 = \frac{1}{N_2^2}\left(P_{|+1>}P_{|-1>} + P_{|-1>}P_{|+1>} + \beta^2 P_{|0>}\right) \tag{2.19}$$

where

$$\alpha = \left(\frac{-A + 2\Gamma + \sqrt{A^2 + 8B^2 - 4AD + 4D^2}}{2B}\right) \tag{2.20}$$

$$\beta = \left(\frac{-A + 2\Gamma - \sqrt{A^2 + 8B^2 - 4AD + 4D^2}}{2B}\right) \tag{2.21}$$

Direct Relaxation Rates

In order to continue our analysis, we must determine the strength of the thermal contact between the NV- center dipolar reservoir and the nuclear Zeeman reservoir. In microscopic terms, this involves a quantum mechanical calculation of transition rates bewteen energy levels using perturbation theory. The following analysis is similar to [47], but adapted to a spin-1 system with a spin-spin splitting. In the previous section we defined the energy levels for a pair of NV- centers coupled through the anisotropic dipolar interaction. We now wish to examine the effect of a single ^{13}C nuclear spin coupled to one of the NV- centers through the dipolar interaction. Since the magnetic dipole of a ^{13}C is on the order of 4000 times weaker than the NV- center, we can treat the influence of the nuclear spin as a perturbation to the Hamiltonian developed in the previous section.

The dipole-dipole interaction between NV- centers and ^{13}C spins is treated as a perturbation that induces transitions between NV- center energy levels. Fermi's Golden Rule gives the direct relaxation rate for a nucleus, m, near a central NV- center, j, which is also coupled to another NV- center, k:

$$W^{jkm} = \frac{2\pi}{\hbar}|\mathcal{V}^{jm}|^2\delta(\Delta E_{13} - \hbar\omega_I) \tag{2.22}$$

$\mathcal{V}^{jm} = \frac{\mu_0}{4\pi}\hbar^2\gamma_{NV}\gamma_I\frac{1}{r^3}(-\frac{3}{2}sin(\theta)cos(\theta)e^{-i\phi})$ is the Hamiltonian matrix element for transition, from $\mathcal{H}_{\mathcal{IS}}$. Angular dependence is removed by spatial averaging to obtain $|\mathcal{V}^{jm}| = -\frac{\mu_0}{4\pi^2}\hbar^2\gamma_{NV}\gamma_I\frac{1}{r^3}$. In order to obtain an average transition rate, a sum over all neighboring NV- centers, k, is approximated as an integral:

$$W^{jm} = \int_{-\infty}^{\infty}\rho(A)g(A)W^{jmk}(A)\,dA \tag{2.23}$$

where g is the normalized distribution of values of A, and $\rho = P_1 + P_3$ is the probability that the NV- center pair is in state 1 or 3. For a dilute spin system, $g(A) = \frac{\delta}{\pi(\delta^2+A^2)}$, where $\delta = \frac{2\pi^2}{3\sqrt{3}}\gamma_{NV}^2\hbar^2 n$ and n is the number density of NV- centers [1]. The integral may then be evaluated:

$$W^{jm} = \sum_{i=1,2}\rho(A_i)W^{jmk}(A_i)g(A_i) \tag{2.24}$$

where A_i are the two roots of the argument of the delta function in W.

Effective Spin Temperature

From the previous section, we can see that only two electron dipolar levels, 1 and 3 are involved in the polarization process. The NV- dipolar energy reservoir system is now simplified to a pseudo two-level system, for which a spin temperature may be defined in a straightforward way (returning to the designations for two NV- center states):

$$T_{spin} = \frac{E_3 - E_1}{k_B \ln(\frac{P_1}{P_3})} \tag{2.25}$$

P_3 and P_1 are the populations of states 3 and 1. As shown previously, the populations depend upon A and γ, the values of which were determined in the previous section, with two possible roots to the delta function for each value of γ. As an example, in the case where $P_{|0>} = 1$, the ratio $\frac{P_1}{P_3}$ becomes zero and the effective spin temperature approaches negative zero, or the zero-entropy state where all members of the ensemble are in the highest energy level.

Spin Diffusion and Transport Model

In the previous section we showed that the direct relaxation rate is proportional to $|\mathcal{V}^{jm}|^2$, which decays as $1/r^6$. Therefore, direct relaxation is only significant for those nuclei sufficiently close to NV- centers. We now turn our attention to the transport of spin polarization from these proximate nuclei to the bulk material. In other words, we will investigate the mechanism by which the nuclear Zeeman energy reservoir establishes internal thermal equilibrium. The average distance between nearest neighbor polarizing NV- centers is [46]:

$$R = \left(\frac{3}{4\pi N_{NV}}\right)^{\frac{1}{3}} \tag{2.26}$$

We define the location of an NV- center to be $r = 0$. The transport of polarization to the bulk material occurs through energy conserving homonuclear flip-flop transitions, known as spin diffusion. We will approximate this process as diffusion in a continuum, even though the spins lie on a discrete crystal lattice. This should be a good approximation when $R >> a$, where a is the average distance between nuclei. A further simplification is made by averaging over all angles so only transport in the radial direction is modeled. The polarization is then modeled using an effective spin diffusion coefficient D_{eff} in conjunction with a well known equation for radial transport in spherical coordinates :

$$\frac{dP}{dt} = D_{eff}\frac{1}{r^2}\frac{d}{dr}(r^2\frac{dP}{dr}) + (P_0 - P)W_{avg}(r) \tag{2.27}$$

where P is the nuclear spin polarization, W_{avg} is the direct relaxation rate calculated in the last section, and P_0 is the thermal equilibrium nuclear polarization at the NV- effective spin temperature. We have neglected spin-lattice relaxation in this treatment.

The initial and boundary conditions are:

$$P(t = 0) = 0 \tag{2.28}$$

$$\frac{dP}{dr}(r=0)=0 \tag{2.29}$$

$$\frac{dP}{dr}(r=R)=0 \tag{2.30}$$

The initial condition represents saturation of the nuclear spins prior to optical pumping, while the boundary conditions follow from symmetry. This equation is solved numerically using Mathematica to obtain polarization as a function of r and t using the literature value $D_{eff} = 6.7 * 10^{-15} \frac{cm^2}{s}$[46]. In order to avoid overflow error due to the $\frac{1}{r^6}$ dependance of $W_i(r)$, the $r = 0$ boundary condition was instead applied at $r = 10^{-12}$m. This value is significantly less than a carbon-carbon bond length, so polarization neglected within this radius is not physically realistic. Using a defect density of $n \sim 10^{19}\text{cm}^{-3}$, the numerical solution was rescaled and superimposed upon data taken at 5K in Fig. 2.3. This model is in good agreement with the characteristic timescale estimated for the diffusion-limited case where $\tau = \frac{R^2}{D}$, which is 69.6s for the values used in this model. It should be noted that after publication [20] it was discovered that an incorrect value for the spin-spin splitting of the 109.5 degree defects was used in the simulation. This should not significantly affect the polarization rate, but does have implications for the spin temperature of those manifolds. A corrected version of the simulations will also include a description of how the population the the NV- Zeeman states varies with the angles of the defect symmetry axes relative to the magnetic field. Since we are still developing an understanding of how the optical pumping process is affected by a large magnetic field misaligned with the defect symmetry axis, this simulation remains as future work.

2.5 Conclusions

Kinetics

We have shown that the timescale for nuclear polarization does not depend on temperature. This is consistent with our model in that the relevant transitions are energy-conserving without energy exchange with the lattice. This is in contrast to other DNP methods such as the Overhauser effect, solid-state effect, and optical nuclear polarization in inorganic semiconductors, all of which depend upon lattice energy to facilitate electron/nuclear transitions. This has several important implications. The timescale of polarization can be much faster than the spin-lattice relaxation rate, especially at low temperatures where the polarization can be preserved long after the optical pumping. Also, this method is not dependent upon the Boltzmann factor to achieve large polarizations, as is the case with microwave-induced DNP methods. Therefore, in sample optimized for slow spin-lattice relaxation, this technique possibly could be used at higher temperatures as well. Additionally, the polarization rate should be highly dependent upon NV- center concentration, allowing for tuning of the polarization kinetics. At the time of this study, only one NV- concentration was available but

studies are currently under way to determine the dependence of the polarization mechanism on NV- concentration.

Temperature Dependence

The dependence of the polarization kinetics on temperature merits further investigation. Earlier we proposed that a temperature-dependent phonon sideband in the optical absorption spectrum may allow greater optical penetration depth at lower temperatures [20]. Our current speculation is that temperature-dependent spin-lattice relaxation processes (such as those involving other paramagnetic defects) compete with and reduce the effectiveness of the optical polarization. The lineshape changes may be due to temperature-dependant behavior of the experimental apparatus, such as magnetic susceptibility of materials or movement of the sample within the magnet due to thermal contraction. However, they may also be an indirect probe of the spin dynamics of paramagnetic defects in the sample. The spin-lattice relaxation times of these defects are highly temperature-dependant and the data may reflect a transition between a "fast spin-flip" regime where the dipolar interaction with the nuclei is averaged and a "slow spin-flip" regime where the defect spins are static on the timescale of the dipolar interaction. Further studies are warranted to investigate this phenomenon.

Chapter 3

Spin Ensemble Thermodynamics of the NV- Center

Introduction

The previous chapter introduced the concept of a dipolar energy reservoir consisting of a dense ensemble of interacting paramagnetic NV- centers. A quantitative description of this mechanism requires knowledge of the spin temperature of this reservoir. In the previous chapter a two-defect system with a distribution of dipolar couplings was used to approximate this energy reservoir. Additionally, we assumed that the state of the ensemble is the tensor product of single-defect states under optical pumping rather than consider evolution of the ensemble under the dipolar interaction. In this chapter we describe preliminary attempts to address these assumptions and a more rigorous, many-spin description of the ensemble spin temperature.

A Microcanonical Ensemble

The stated goal of this section is to determine the spin temperature of the NV- ensemble. However, in assuming that a well-defined spin temperature exists we have implicitly assumed that the dipolar energy levels of the ensemble have reached an internal equilibrium (i.e. thermalization). This is in contrast to the previous "Toy Model" where we assumed the ensemble was optically pumped in to a particular state which does not evolve until interaction with the nuclear spins. The time scale for thermalization among dipolar energy levels is identical to the spin-spin relaxation time, or T_2 (assuming that the spin-spin dipolar interaction is the dominant mechanism in determining T_2.) Literature values for T_2 for samples of similar NV- density to the ones in this work indicate this thermalization happens on the timescale of microseconds [45]. We must then compare this timescale to that for re-initialization of the NV- spin state by optical pumping. Unfortunately, this value is not readily available and most likely depends on the intensity of the illumination, polarization of the illumination, and penetration depth of the illumination. So, while we proceed with this analysis assuming

that the spin ensemble is indeed thermalized, future researchers should keep in mind the questionable validity of this assumption.

Now that we are working with an equilibrium state, we can use the thermodynamic definition of temperature:

$$T = \frac{dE}{dS} \tag{3.1}$$

Since the spin system is energetically isolated (T_1 is long), it is appropriate to work with the microcanonical ensemble. The entropy is then:

$$S = k \ln \Omega(E) \tag{3.2}$$

where $\Omega(E)$ is the number of microstates with a given energy E. Keeping in mind from the previous chapter that we are only concerned with transitions for which $\Delta S_z = 0$, we can neglect the Zeeman Hamiltonian in this calculation (although its influence is still present through the neglect of Hamiltonian terms with which it does not commute). We also recognizing the dipole-dipole interaction is small relative to the internal spin-spin splitting of the NV- center. As an example, we consider the case for which total S_z of the ensemble is equal to zero (the same as assuming the $+1$ and -1 states are populated equally). The number of ways an N-spin ensemble can be configured to give an energy E is:

$$\Omega(E) = \frac{N!}{(N - \frac{E}{D(\theta)})!(\frac{E}{2D(\theta))})!^2} \tag{3.3}$$

where D(θ) is the component of the spin-spin splitting that commutes with the Zeeman Hamiltonian. θ is the angle between the defect symmetry axis and the laboratory z-axis. In order to apply this theory to a quantitative model of the orientation dependence of nuclear polarization, we must know the angular dependence of secular part of the spin-spin splitting D. The spin-spin hamiltonian transforms under rotation like a rank-2 tensor, so the angular dependence of the splitting is given by the following Wigner matrix element:

$$d^2_{0,0} = \frac{1}{2}(3\cos^2\theta - 1) \tag{3.4}$$

This symmetry may be familiar to NMR researchers as it has the same form as the Hamiltonian for the nuclear electric quadrupole moment interacting with an electric field gradient. So we have:

$$D = h * 2.88GHz\frac{1}{2}(3\cos^2\theta - 1) \tag{3.5}$$

The energy of the system is entirely due to the internal spin-spin splitting and is equal to:

$$E = ND(\theta)(\frac{1}{3}P_{+1} + \frac{1}{3}P_{-1} - \frac{2}{3}P_{+1}). \tag{3.6}$$

Now, we can directly calculate the entropy:

$$s = k \ln \frac{N!}{(N - \frac{E}{D})!(\frac{E}{2D})^2!}. \tag{3.7}$$

This expression poses a problem since it is not a continuous function of energy, as will be needed to calculate the temperature. One option is to use Stirling's approximation for logarithms of large factorials and assume $N >> 1$, $N >> \frac{E}{D}$, and $\frac{E}{D} >> 1$. This yields the following expression for entropy:

$$s \sim k(N \ln N - (N - \frac{E}{D}) \ln(N - \frac{E}{D})). \tag{3.8}$$

Another approach is to recognize that the expression for Ω closely resembles a Gaussian curve (the combinatorial expression resembles a binomial distribution, which may be approximated as a Gaussian function in certain limits). However Ω, and therefore entropy, is approximated as a continuous function of E, the spin temperature may be defined as a derivative:

$$1/T = \frac{dS}{dE}. \tag{3.9}$$

In making this analysis, we assumed a collection of discrete energy levels behaves as a continuum. This is valid if the homogeneous broadening due to the dipole-dipole interaction is sufficient. However, since this broadening is known to be of the order of 10 MHz, and the splitting between energy levels can be as large as 2.88 GHz, the validity of this assumption remains open to questioning. Another possibility is that it is not a single continuum of states that participates in the heat exchange, but many manifolds of states separated by $2D(\theta)$ each form a continuum. Such a mechanism would not require an energy gap on the order of GHz ($2D(\theta)$) to be overcome in order to couple to the nuclear spins. However, this also means there are many different energy reservoirs (each characterized by a constant $\sum S_z^2$) with separate spin temperatures. We have yet to develop a tractable solution for this theory

3.1 An Ensemble not at Equilibrium

As mentioned in the previous section, we do not yet know if the assumption of internal equilibrium is valid, so we must consider the possibility that no well-defined spin temperature exists among the dipolar energy levels of the spin ensemble. This is similar to the 2-spin "Toy Model" presented in the last chapter but extended to a system with many energy levels, rather than just 2. In the 2-spin model, we reduced the number of relevant NV- states to 2, and it is a particular quality of 2-level systems that they always have a well-defined spin temperature, something that will not be the case in a many-spin solution. A many-spin solution will require the calculation of population distributions among the many dipolar energy levels as well as the transition rates for each pair of levels based on the available density of states. Such a treatment will require theoretical methods beyond what have been employed here.

Chapter 4

Electric-Quadrupole Induced Nuclear Polarization in Gallium Arsenide

4.1 Introduction

Optical control of nuclear polarization in semiconductors has been an active area of research for a community comprised of both nuclear magnetic resonance (NMR) spectroscopists and condensed matter physicists[15]. As a probe of electron-nuclear interactions in the presence of spin-couplings, such control is interesting at a fundamental scientific level. There is also considerable interest in applying optical control of nuclear spin polarization to sensitivity-enhanced NMR[24] and devices for quantum information processing[8][44]. Control of the sign and magnitude of the polarization, especially as a function of position, is an important prerequisite for proposed devices[36][42]. The most studied and best understood material is gallium arsenide (GaAs). Optically-pumped NMR (OPNMR) in GaAs has been explained by invoking a model where spin-polarized electrons are excited and spin exchange occurs with electrons bound at shallow donors[6][32]. These bound, spin-polarized electrons then polarize proximate nuclei primarily through the Fermi-contact hyperfine interaction.

The energy dependence of the OPNMR signal amplitude in GaAs exhibits several general features. Far above the bandgap, the sign of the OPNMR signal may be controlled with the light helicity and the spectrum exhibits oscillations as a function of photon energy due to the appearance of Landau levels[27]. Near the bandgap, a maximum in the OPNMR signal is observed due to the interplay of photon penetration depth and electron spin polarization[6]. Below the bandgap, a different regime emerges where the OPNMR signal can no longer be controlled with light helicity and always assumes a positive value with respect to thermal polarization, suggesting a different polarization mechanism is at work (Fig. 1). Previous studies have proposed mechanisms, perhaps involving an electronic species with a positive g-factor[34], but none have attempted to model this regime, nor have they provided experimental tests of these mechanisms.

In this chapter, we present experimental data showing the dependence of OPNMR signal

on incident laser intensity, rather than photon energy. We identify a regime at low laser intensity with similar phenomenology to the previously observed regime of low photon energy. We show that both situations are explained by including the effects of both quadrupolar and electron-nuclear hyperfine relaxation on the growth and decay of the observed bulk OPNMR signal. The rates of both relaxation mechanisms are determined by the free electron concentration and shallow donor occupation fraction, which vary throughout the depth of the sample. These parameters are determined at a given laser intensity and photon energy by the optical absorption spectrum for GaAs.

4.2 Results

OPNMR spectra of ^{71}Ga, as well as ^{69}Ga and ^{75}As, were collected for a bulk semi-insulating GaAs wafer (American Crystal Technologies) 350 μm in thickness, surface orientation [100], resistivity greater than $10^7\Omega$cm, mobility greater than 6000 $\frac{cm^2}{Vs}$, in a 9.4 T magnetic field at low temperature. The sample was placed in a continuous flow cryostat and in good thermal contact with a sapphire wafer to facilitate heat transfer at 6 to 8 K. NMR detection was preceded by the rf pulse sequence $SAT - \tau_L - \tau_D - \frac{\pi}{2}$, where τ_L and τ_D indicate illumination and dark intervals, which were 180 s and 10 s respectively, unless otherwise noted. Saturation (SAT) prior to illumination was carried out via a series of $\frac{\pi}{2}$ pulses. The beam diameter was ~ 1.5 mm.

Figure 2 shows the dramatic change in observed NMR polarization for ^{71}Ga when the laser intensity is decreased to $\approx .83$ μW/cm at 1.503 eV. At this photon energy, none of the previously published models [26] can account for this pronounced loss of sensitivity to light helicity. A new mechanism for optically-induced NMR effects is therefore suggested. Previous workers have developed a model to explain the reduction of OPNMR signal by quadrupolar-induced depolarization [31]. Here, we consider quadrupolar relaxation as a mechanism for polarization which, in certain regimes, may dominate over hyperfine polarization and reverse the sign of the NMR signal. Quadrupolar relaxation occurs near shallow donors as the capture, release, and recombination of electrons creates a fluctuating electric field gradient[31]. These fluctuations are governed by the kinetic temperature of the electrons, and therefore drive the nuclear spins to this temperature, with no dependence on the electron spin polarization. The equilibrium spin temperature achieved by quadrupolar relaxation results in a spin polarization which has the same sign as the thermal equilibrium spin polarization.

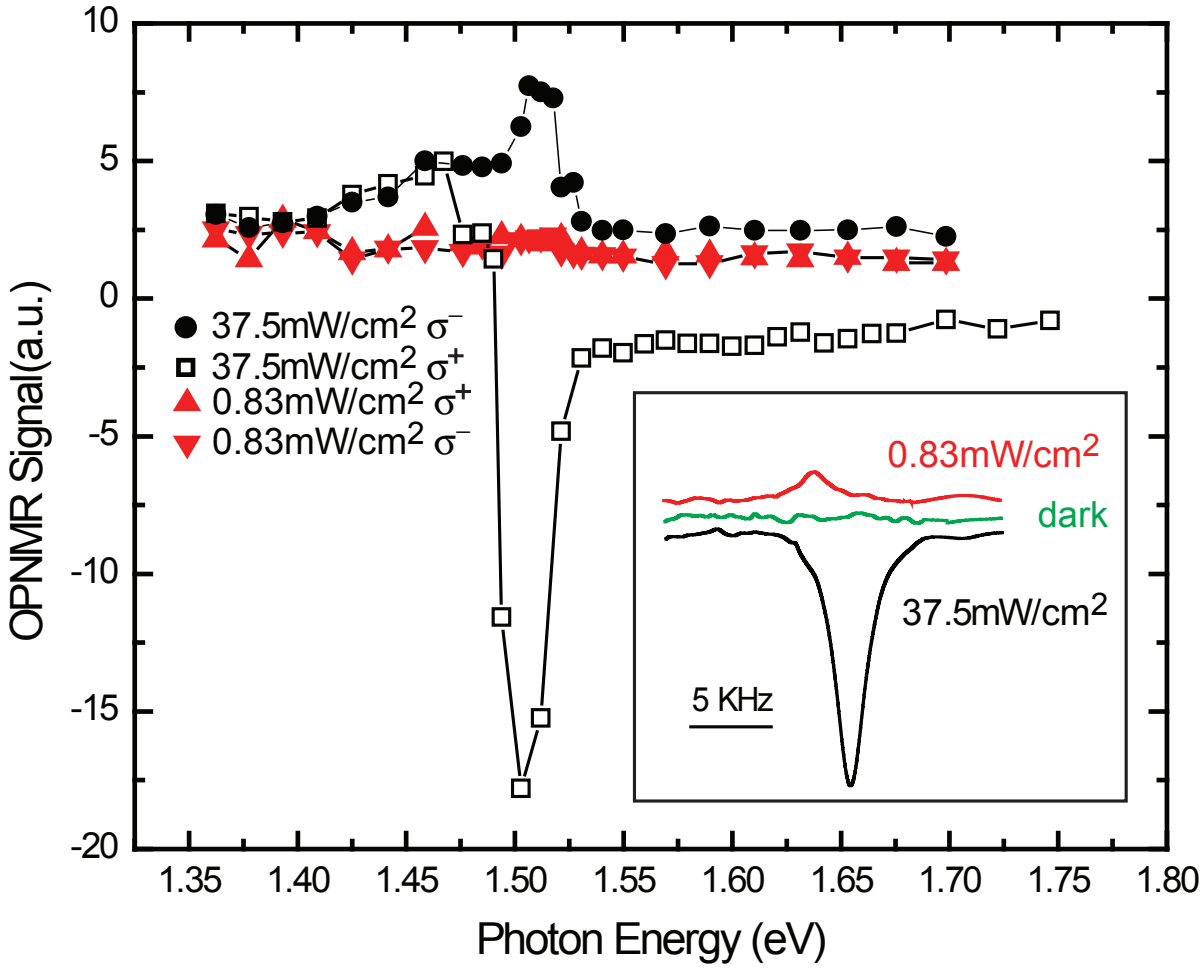

Figure 4.1: OPNMR profile for ^{71}Ga in GaAs, showing helicity-independent signal with positive NMR signals for low photon energy and for low laser intensity. Temperature is 8 K. (From [22].)

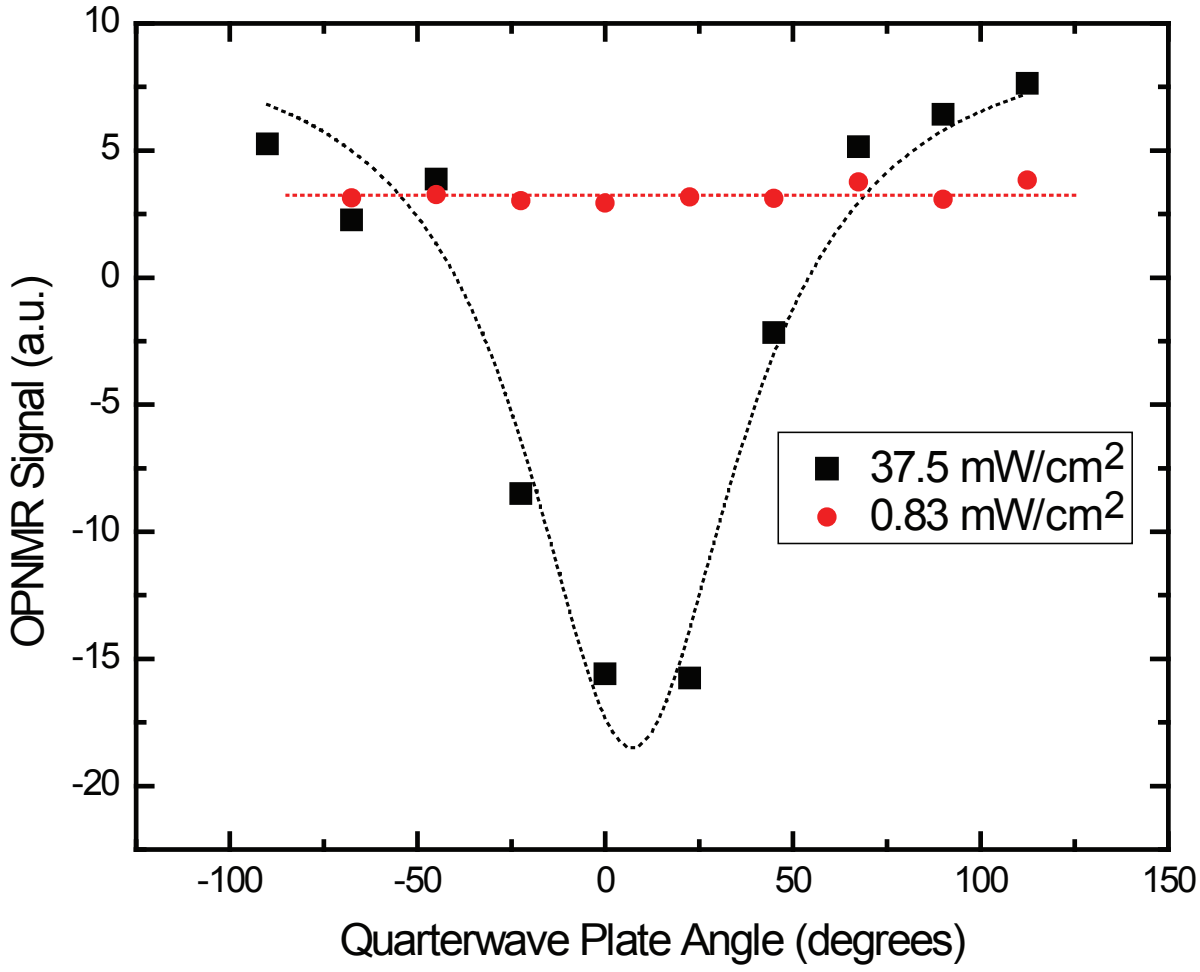

Figure 4.2: Optically enhanced signal for ^{71}Ga as a function of light helicity at different laser intensities. The temperature was 6 K. The beam diameter was 1-2 mm. The laser wavelength was 1.503 eV. $\tau_D = 10$ s and $\tau_L = 180$ s. The dotted lines are guide for eye only. (From [22].)

4.3 Discussion

The important parameter in a model [31] for OPNMR when nuclear spins possess a quadrupolar moment is the ratio of the two relaxation timescales, f, defined by:

$$f = \frac{T_{1,Q}}{T_{1,H}} \ , \tag{4.1}$$

where Q and H stand for quadrupolar and hyperfine relaxation. f is found to be a function of the donor occupation fraction, Γ, and in the high magnetic field limit, this dependence is given by:

$$f = f_0 \frac{\Gamma}{1-\Gamma} \ . \tag{4.2}$$

Previous works have primarily studied the regime of high laser intensity and near to above-gap irradiation. In this case, Γ is close to one, f is large, and the hyperfine mechanism dominates. Here we consider the case where the donor occupation is less than one, either due to lower laser intensity or reduced absorption at low photon energies.

f_0 is a property of the material and nucleus under investigation. By observing 3 different nuclei in the same sample, we can isolate the effects of varying the gyromagnetic ratio, γ_N, and the product of the quadrupolar moment and electrostatic antishielding, QR_{14}[31]. f_0 scales as:

$$f_0 \propto \frac{\gamma_N^2}{Q^2 R_{14}^2} \ , \tag{4.3}$$

Based on this scaling behavior, we expect the transition from quadrupolar-dominated to hyperfine-dominated behavior to occur at increasing values of laser intensity in the order ^{71}Ga$<^{69}$Ga$<^{75}$As. This trend is clearly seen in Figure 3, supporting the proposed mechanism.

It was discovered previously that laser penetration depth effects have a significant impact on the OPNMR signal [6, 26]. Our analysis predicts that not only can the magnitude of $\langle I_z \rangle$ vary throughout the depth of the sample, but the sign of $\langle I_z \rangle$ may vary as well. Qualitatively, for high laser intensity and near to above gap irradiation, the majority of the light is absorbed near the surface of the sample, with a high donor occupation fraction and free electron concentration. The OPNMR signal is then almost entirely due to this region where hyperfine relaxation is dominant. As the photon energy is lowered well below the bandgap, the penetration depth becomes large, the rate of absorption per unit volume is much lower and is spread throughout a larger region of the sample. In this case, the OPNMR signal is due to a large region of the sample with lower donor occupation fraction and free electron concentration where quadrupolar relaxation dominates. This accounts for the behavior in the low photon energy regime that was previously unexplained[34].

For near and above gap irradiation, the OPNMR signal will always be limited to the region near the surface due to small penetration depths. By reducing the laser intensity, however, the free electron concentration and donor occupation fraction in this region may be

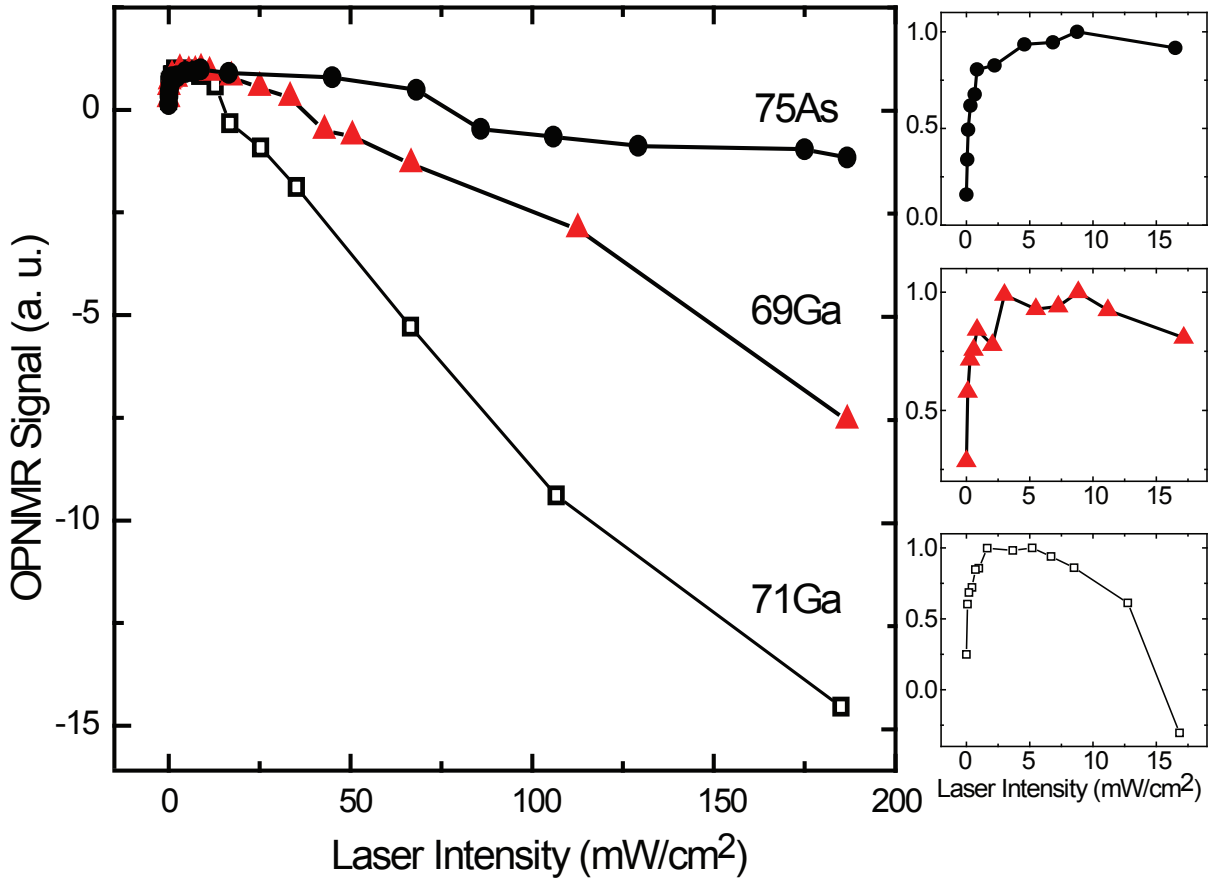

Figure 4.3: OPNMR signal as a function of laser intensity for ^{71}Ga (circles), ^{69}Ga (squares), and ^{75}As (diamonds). Photon energy is 1.503 eV. Temperature is 6 K. (From [22].)

lowered so that quadrupolar relaxation dominates. There also exists an intermediate case for both laser intensity and photon energy where the net OPNMR signal is zero. This analysis suggests that in this case $\langle I_z \rangle$ is not zero throughout the sample, but rather there are regions of positive and negative $\langle I_z \rangle$.

We have experimentally demonstrated a new, helicity-independent regime of OPNMR at low laser intensity. These data are consistent with competing hyperfine and quadrupolar relaxation mechanisms, including scaling behavior for different nuclei. This physical picture also accounts for the previously unexplained regime of low photon energy. These competing mechanisms provide a means by which to pattern nuclear polarization on a sub-micron length scale by adjusting photon energy and laser intensity. This patterning is an important step in the development of devices using hyperpolarized nuclear spins.

Chapter 5

Patterned Nuclear Magnetism in Gallium Arsenide

5.1 Introduction

Control of electron spins in semiconductors impacts the design and analysis of both solid-state quantum computation schemes and spintronics devices[48, 30]. In both applications the electron spins are subject to internal magnetic fields that arise from nuclear spins. The small energy separation between nuclear spin states leads to a highly disordered, fluctuating spin ensemble that contributes significantly to electron spin decoherence, thereby limiting the fidelity of quantum computation. If the nuclear spins are polarized, their magnetic field acts on electron spins to produce an effective, static field in addition to the fluctuating component. Spatial control of this internal field is a prerequisite to coherent control of electron spin currents in spintronics devices[19]. While patterns have been imprinted via ferromagnetic heterostructures[41, 43], and nanometer-scale control has been achieved by a variety of methods in quantum-confined semiconductors[35, 28], no general scheme for controlling internal nuclear fields has yet been developed for unstructured, bulk semiconductors.

Optical excitation for the crafted preparation of nuclear polarization $\bar{I}_z$ in semiconductors has a history extending back several decades[15]. Previous work focused on the selection rules for excitation of spin-polarized electrons in GaAs, and the subsequent exchange of these electrons with spins bound at recombination centers[33]. These bound electrons have a strong contact hyperfine interaction with nearby nuclei which undergo dynamic nuclear polarization (DNP) driven by spin exchange modulation of the hyperfine field. The DNP rate decays exponentially with distance from the recombination center, and scales linearly with probability of trapping at a recombination center[6, 26]. Both the magnitude and sign of the polarization of nuclei undergoing DNP may be controlled by the polarization of the incident light. In the previous chapter we identified a second mechanism[22, 31] for nuclear polarization that arises from the interaction of a nuclear electric quadrupole moment with fluctuating electric field gradients at a recombination center. These gradients arise from the

spin exchange process at recombination centers and result in a positive nuclear polarization by facilitating thermal relaxation.

The charge carrier dynamics that drive both polarization processes depend upon optical absorption rate, which is a function of optical absorption coefficient and light intensity. In the regime (near to above gap) where the optical penetration depth is smaller than the sample thickness, the electron generation rate is strongly dependent upon depth in the sample. Because both illumination intensity and penetration depth (via different wavelengths) are variable across several orders of magnitude in typical laboratory settings, these parameters may be used to "tune" the recombination center dynamics and control the sign and magnitude of nuclear polarization. Here we harness this control to create micron-scale patterns of nuclear polarization as a function of position and isotope. These patterns are easily re-writable, depend only on simple parameters of optical excitation, and may be easily manipulated with NMR pulse sequences.

5.2 Results

Internal Nuclear Fields

An intuitive way to view how nuclear polarizations produce effective static fields for spintronics applications begins with the Hamiltonian governing the behavior of electron spins in a semiconductor:

$$H = g\mu_B S \cdot B + \sum_{n=1}^{N} A_n S \cdot I_n \tag{5.1}$$

The first term of this Hamilltonian is associated with the static field and applied resonant pulses. The second term represents the contact hyperfine interaction with the many (N) nuclei enveloped by the single electron wavefunction. We can separate the applied magnetic field, B, into its static z-component (the Zeeman field denoted B_0), and its time dependent component (RF or microwave pulses, arbitrarily chosen to be along the x-axis). We can also separate the hyperfine interaction with nuclei into a static component (which has non-zero magnitude only in the z-direction) and a fluctuating component:

$$H = g\mu_B S_z B_0 + g\mu_B S_x B_x(t) + \bar{A} S_z \bar{I}_z + \sum_{n=1}^{N} A_n S \cdot \delta I_n(t). \tag{5.2}$$

Control of the average nuclear polarization, $\bar{I}_z$, effectively controls the Zeeman field as a function of position in space

$$H = g\mu_B S_z B_{eff}(\overrightarrow{x}) + g\mu_B S_x B_x(t) + \sum_{n=1}^{N} A_n S \cdot \delta I_n(t) \tag{5.3}$$

with $B_{eff} = B_0 + \frac{\bar{A}\bar{I}_z(\overrightarrow{x})}{g\mu_B}$. It is this spatially-dependent field that will enable spintronic and quantum computing device technologies and experimental control of $\bar{I}_z(\overrightarrow{x})$ is the necessary prerequisite.

In order to understand how control of $\bar{I}_z(\overrightarrow{r})$ can be used to create patterns of nuclear magnetization, we examine the two distinct mechanisms of nuclear polarization. The hyperfine-induced nuclear polarization rate by the electron spin-exchange mechanism in the high-field limit is[31]

$$\frac{1}{T_H} \propto \frac{\Gamma\gamma_N^2 e^{-4\frac{r}{a_0}}}{\omega_H^2 \tau_H}, \tag{5.4}$$

where a_0 is the Bohr radius, Γ is the probability of a trapped electron at a recombination center, r is the distance of a nucleus from the recombination center, γ_N is the nuclear gyromagnetic ratio, τ_H is the correlation time for fluctuations of the hyperfine field, and ω_H is the frequency associated with a nuclear-electron "flip-flop" transition.

In contrast, the quadrupolar polarization mechanism occurs due to modulation of the electric field gradients (EFG's) around recombination centers. These modulations are caused by the alternation between the ionized and neutral state of the recombination center due to electron capture and recombination[31]. This modulation couples the nuclear Zeeman energy reservoir to the kinetic energy reservoir of the electrons, which rapidly equilibrates with lattice phonons [49]. Therefore, this mechanism always drives nuclei towards a positive spin temperature. The angular and radial dependence of the polarization rate are subtle, but in the high field limit the angular dependence of the total relaxation rate disappears and the rate is given by[31]

$$\frac{1}{T_Q} \propto \Gamma(1-\Gamma)\frac{s^2(r)}{r^4}\frac{R_{14}^2 Q^2}{\omega_N^2 \tau_Q}, \tag{5.5}$$

where Q is the quadrupolar moment of the nucleus, R_{14} is the electrostatic antishielding factor, ω_N is the NMR frequency, and τ_Q is the correlation time of fluctuations of the EFG's. The radial factor $s(r)$ is given by $s(r) = 1 - (1 + 2\frac{r}{a_0} + 2\frac{r^2}{a_0^2})e^{-2\frac{r}{a_0}}$. For this mechanism the optimum recombination center occupation probability is 50% and the rate decreases to zero as Γ approaches unity.

Defining the ratio of the two relaxation timescales as
and using[31] $\frac{\tau_Q}{\tau_H} \propto \Gamma$, we have (see Eqns. 10-16)

$$f \propto \frac{\Gamma}{1-\Gamma}\frac{Q^2 R_{14}^2}{\gamma_N^2}. \tag{5.6}$$

From this relationship, we model the transport of nuclear spin polarization around a given recombination center as:

$$\frac{\partial I_z}{\partial t} = \frac{1}{T_H(r)}\Big(I_{H,0} + \frac{I_{Q,0}}{f(r)}\Big) - \frac{I_z}{T_H(r)}\Big(1 + \frac{1}{f(r)}\Big) + D\nabla^2 I_z. \tag{5.7}$$

where $I_{Q,0}$ is the equilibrium nuclear spin polarization via the quadrupolar mechanism and $I_{H,0}$ is the steady-state polarization due to the hyperfine mechanism (See Eqns. 17-19). Spin diffusion (characterized by the diffusion coefficient D) is fast relative to the direct polarization rate outside the Bohr radius, where the magnitude of the electron wavefunction is negligible, so gradients of I_z are neglected and the last term in Eqn. 8 is zero. Integrating all terms in Eqn. 8 over the sphere associated with a single recombination center ($R = (\frac{3}{4\pi N_D})^{\frac{1}{3}}$) gives the polarization per recombination center. Since both polarization rates are very small as r approaches R, we approximate the limit of this integral as $R \to \infty$. Equation 8 then yields the solution for polarization per unit volume.

Stray-Field Imaging

NMR imaging is a well-established technique which maps spatial information to the frequency domain by means of a magnetic field gradient. Nuclear spins at different positions within the inhomogeneous field may be identified by their different NMR frequencies. Here we employ a one-dimensional imaging technique known as Stray-Field Imaging (STRAFI)[25]. The STRAFI experiment makes use of the large gradients available in the stray field of a superconducting NMR magnet. A schematic of the experimental setup is shown in Fig. 5.1. With a natural NMR linewidth of approximately 4kHz for ^{69}Ga and a gradient of approximately 19 T/m, we achieved spatial resolution in the z-direction of 20 microns. As shown in the pulse diagram of Fig. 1, data are acquired by first saturating the spin transitions with a series of RF pulses, after which the sample is illuminated with circularly polarized near-gap irradiation followed by signal acquisition via a $\frac{\pi}{2}$ pulse and inductive detection of the transverse magnetization.

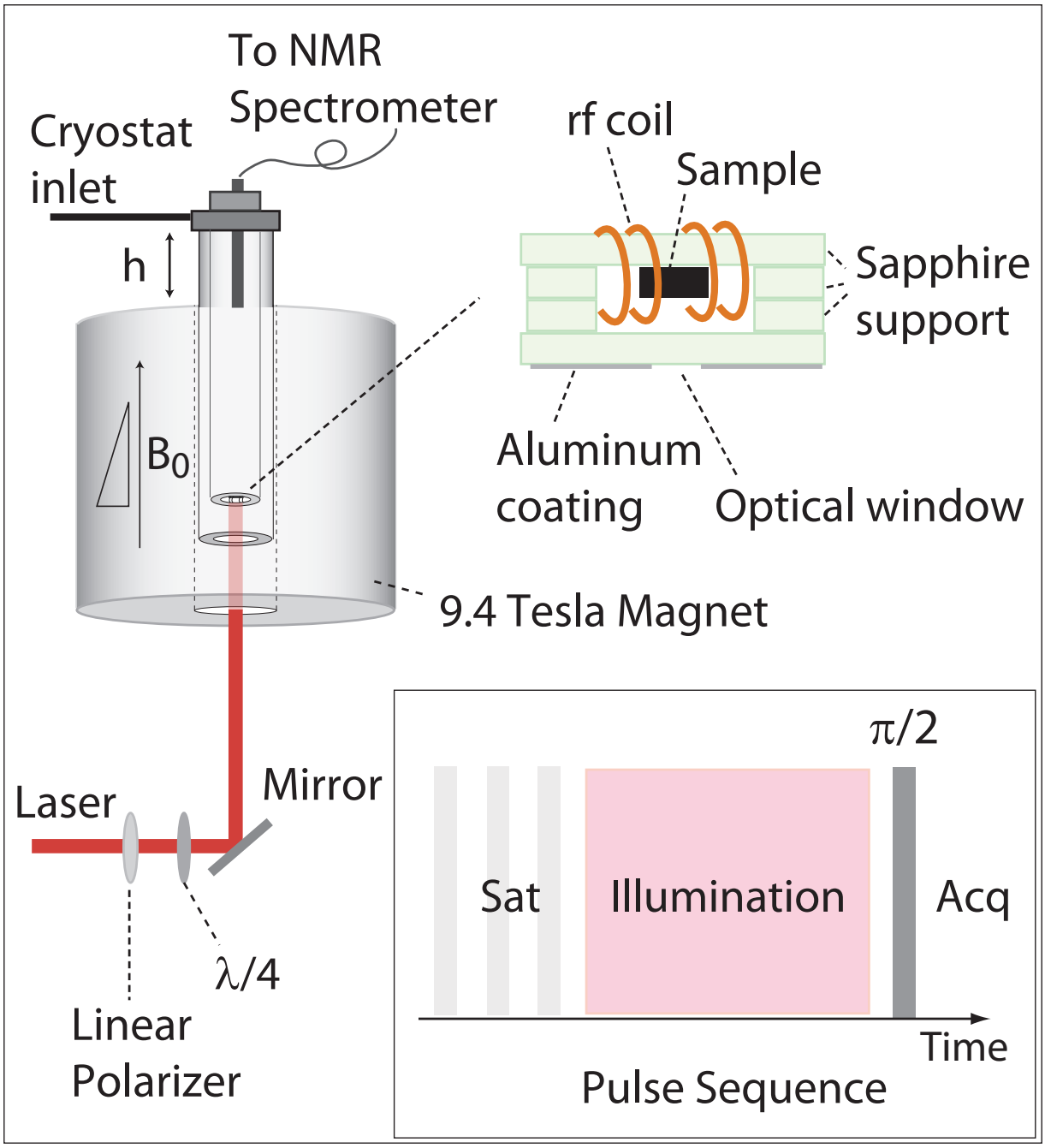

Figure 5.1: Stray-Field Apparatus for Imaging Nuclear Magnetism

The strong gradient in the stray field of a superconducting magnet provides the means for NMR imaging in 1-dimension. Circularly-polarized illumination is directed to the sample through an optical window on the sapphire sample support. Inset: the NMR pulse sequence including saturation, illumination, and detection. (From [21].)

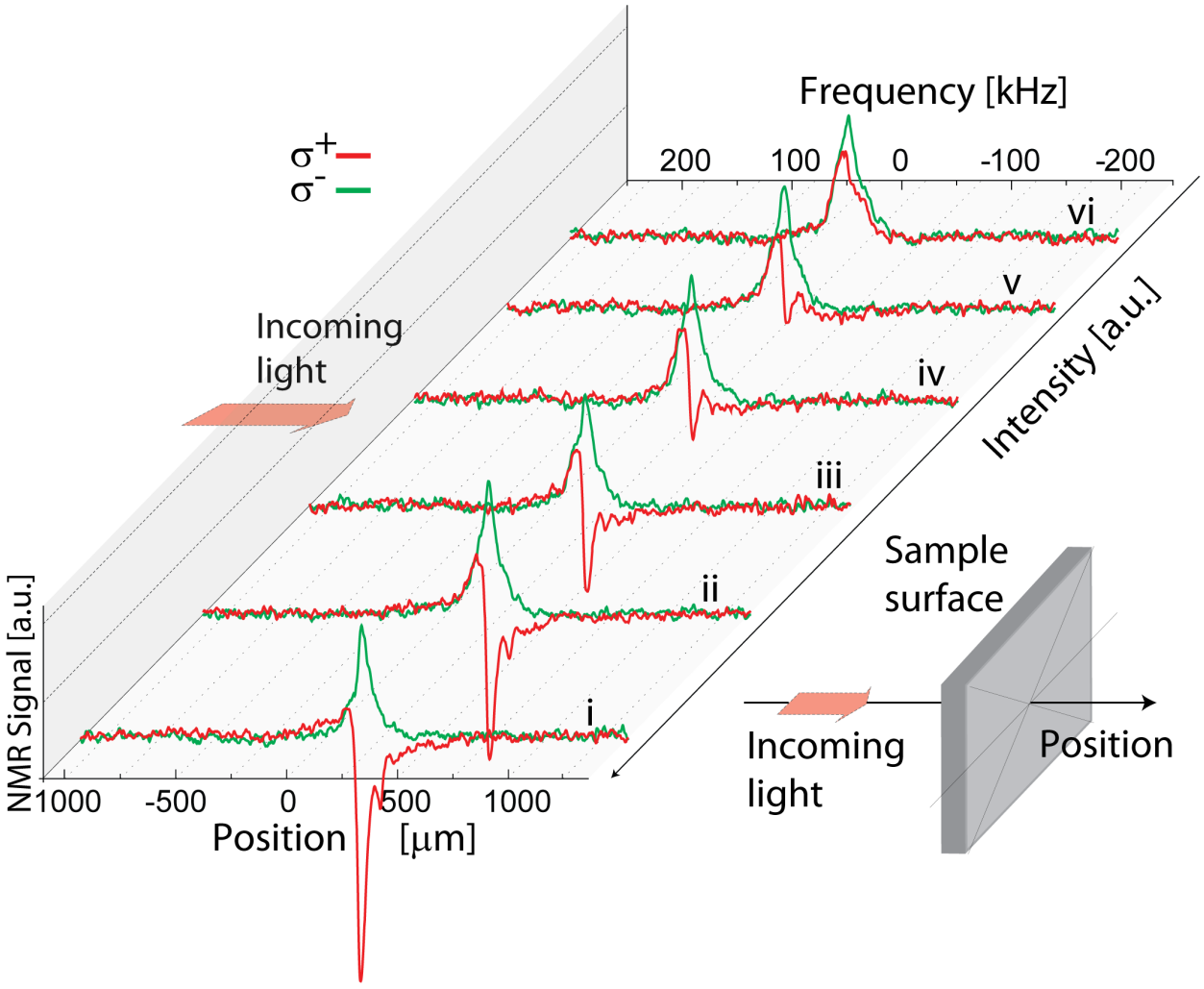

Figure 5.2: Spatial patterns of ^{69}Ga Nuclear Magnetism as a Function of Laser Intensity

NMR images of ^{69}Ga Nuclear Magnetism at (i) 102 mW/cm^2, (ii) 51 mW/cm^2, (iii) 37 mW/cm^2, (iv) 29 mW/cm^2, (v) 12 mW/cm^2 and (vi) 4 mW/cm^2. Red curves correspond to $\sigma+$ helicity and green curves correspond to σ-. The origin is chosen to approximately coincide with the semiconductor wafer surface. Inset: Incoming light illuminates the sample from the left (coincident with higher frequencies in our setup, see upper horizontal axis). (From [21].)

The STRAFI data in Fig. 5.2 correspond directly to the sign and magnitude of nuclear magnetization as a function of depth in the sample. At the lowest illumination intensity (4 mW/cm^2), the polarization is positive throughout the sample, and is nearly independent of helicity, consistent with the bulk experiments reported previously[22]. At the highest illumination intensity (102 mW/cm^2) the sign of the polarization throughout much of the sample may be controlled with light polarization, consistent with many previous bulk studies in

this regime[15, 36]. Here, the intermediate regime is of interest. In this regime of intermediate illumination intensity, using σ^+ polarization, regions of opposite spin polarization are created within close proximity in the GaAs wafer. Neglecting for now the positive signals immediately at the illuminated surface (discussed later) a negative signal is found close to the surface of the sample where absorption is greatest and electron spin-exchange dominates the nuclear polarization process. A positive signal emanates from that portion of the wafer where the light intensity has decayed. In these regions of reduced absorption, the recombination center occupation fraction decreases such that the quadrupolar polarization mechanism is dominant. By adjusting the wavelength of light (Fig. 5.3), we vary the optical penetration depth, controlling the length scale of the patterns of polarization. For example, using 810 nm irradiation our analysis reveals that we created features approximately 40 microns wide.

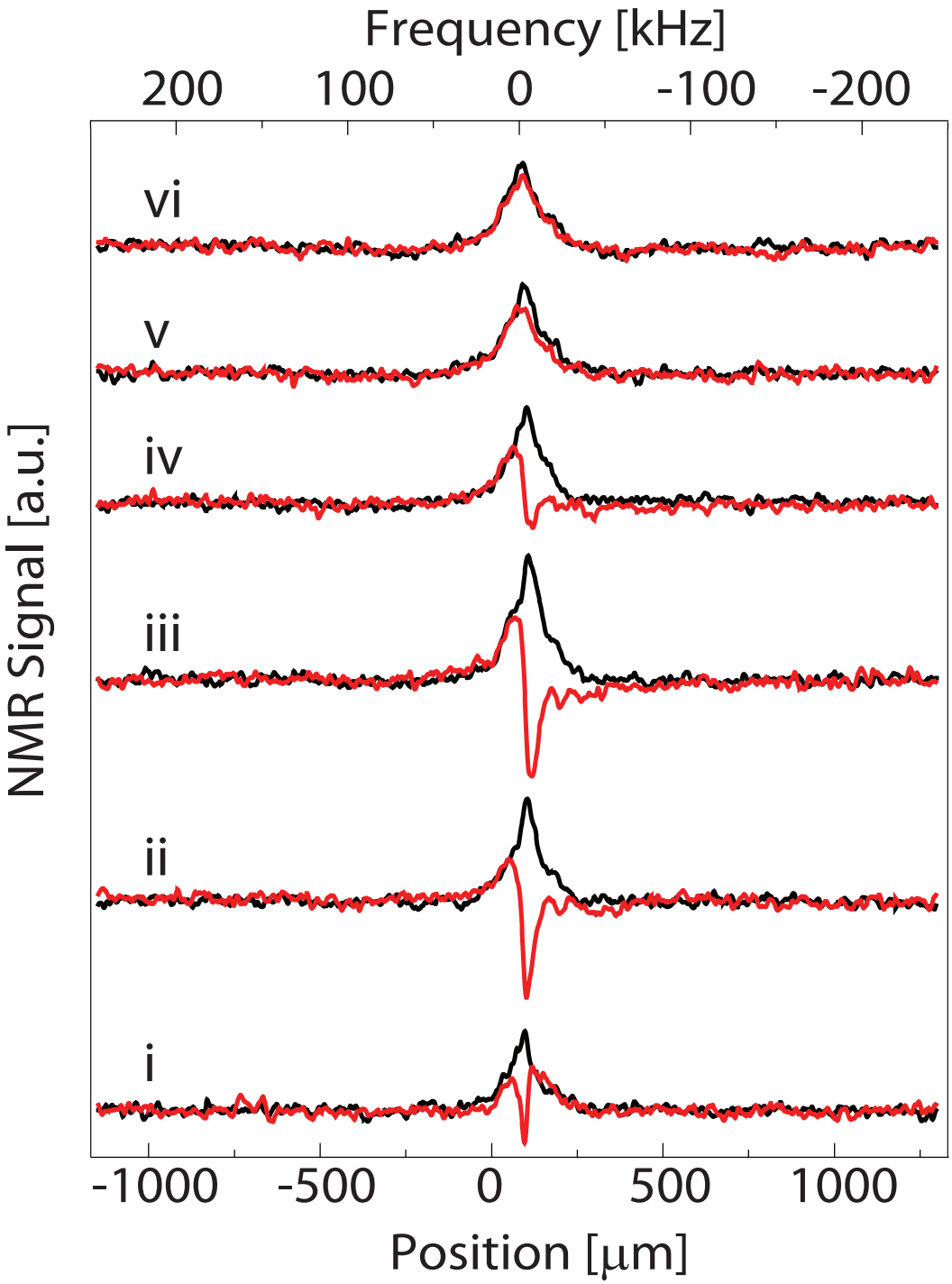

Figure 5.3: Controlling the Length Scale of Nuclear Magnetism with Illumination Wavelength

Stray Field Images of nuclear polarization for ^{69}Ga as a function of irradiation wavelength for an illumination intensity of 37 mW/cm^2 after 10 min. (i) 810nm, (ii) 820nm, (iii) 825nm, (iv) 830nm, (v) 835nm, (vi) 855nm. Red curves correspond to $\sigma+$ helicity and black curves correspond to σ-. Decreasing the wavelength to 810nm (i) provides the shortest length scale for polarization patterning. Our analysis indicates that the width of the negative polarization region associated with this spectrum is approximately 40 microns. (From [21].)

Modeling

Without detailed knowledge of the electron recombination dynamics, optical absorption at high-field and low temperature, and kinetics of electron capture at recombination centers, it is difficult to quantitatively model the dependence of the patterns on illumination wavelength and intensity. However, assuming a single binary recombination mechanism and Langmurian binding of free electrons to recombination centers, combined with literature values for optical absorption[6], we reproduce the shape of the STRAFI images as a function of illumination intensity for a given wavelength (Fig. 4). We also note that for most experimental conditions there is a region of positive polarization localized at the irradiated surface. We attribute this to a depletion layer of low recombination center occupation near the surface where the quadrupolar mechanism dominates. Briefly, defect states pin the Fermi-level mid gap at the surface and an electric field extends from the surface into the bulk. Recombination centers may be ionized in the regions where the electric field exceeds $\sim$ 5000 V/cm[9]. The approximate width of the depletion layer is given by[49]:

$$L = (\frac{2\epsilon\epsilon_0\phi_0}{\rho})^{\frac{1}{2}}, \tag{5.8}$$

where ϵ is the dielectric constrant, ϵ_0 is the vacuum permittivity, ϕ_0 is the potential of the pinned Fermi-level at the surface, and ρ is the charge carrier density. In order to theoretically reproduce STRAFI images, a depletion layer of 50 μm was included in the simulations. Assuming the Fermi-level is pinned mid-gap, this corresponds to a carrier concentration of $\sim 10^{14}$ cm^{-3}, which is similar to the free electron concentrations predicted by the simplified model for a semi-insulating sample at low temperature with optical illumination. Given this very simplistic model, the agreement with experiment (Fig. 5.3) is nearly quantitative.

Engineered Nuclear Magnetization

We investigated the isotope dependence of the patterning process (Figs. 4a and 4b). As expected, the isotope with the larger quadrupole moment and smaller gyromagnetic ratio required greater irradiation intensity to transition from positive to negative polarization. Comparing the intermediate irradiation intensity data in Figs. 5.4a and 5.4b (for example 14 mW/cm^2), we observed the unique situation where different isotopes of the same chemical species have opposite polarization at the same location in the sample, suggesting the ability to create heteronuclear spin order via dipolar or indirect J-coupling[11].

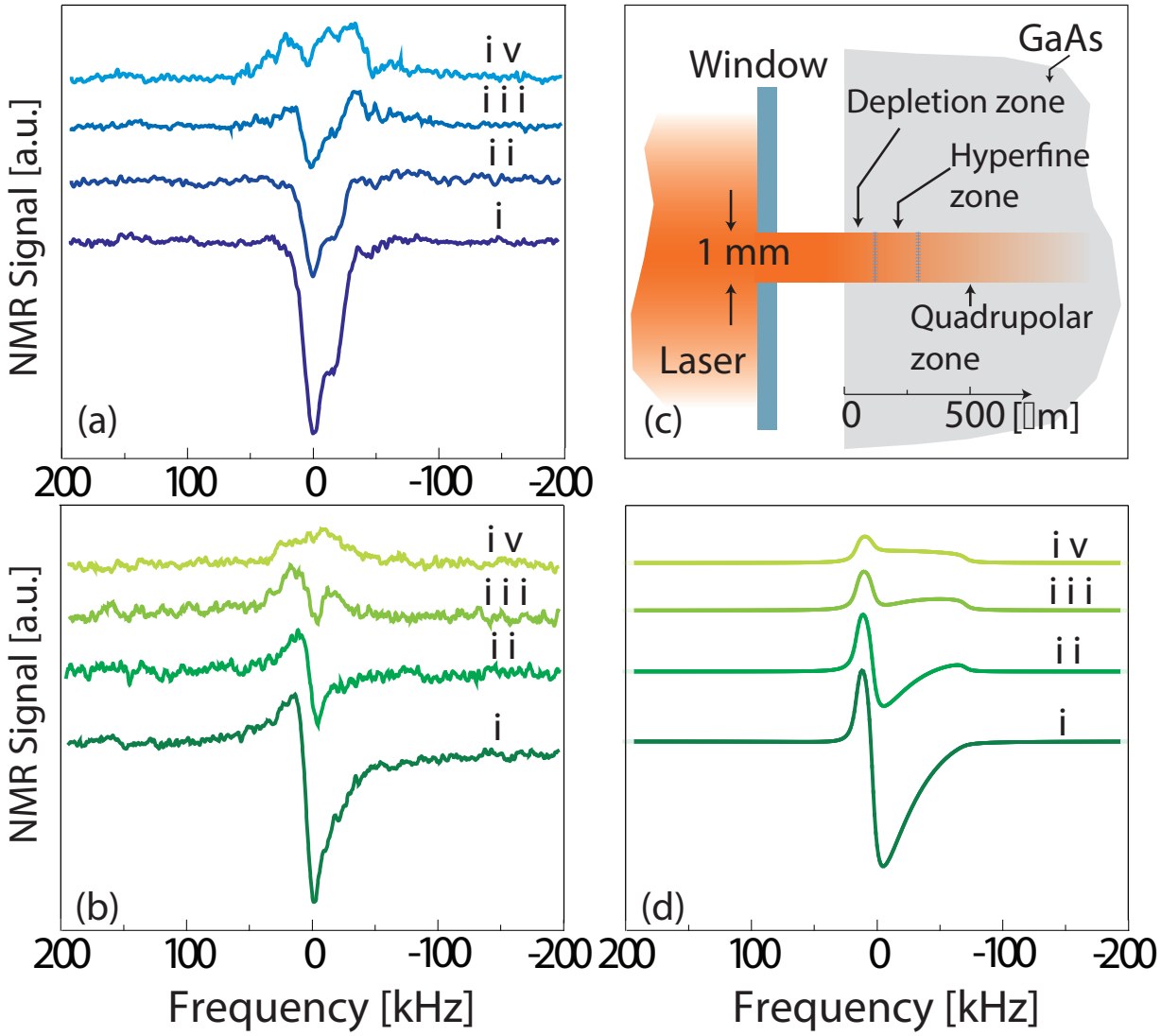

Figure 5.4: Understanding the Roles of Quadrupolar and Hyperfine Polarization.

Stray Field Images of nuclear polarization for (a) ^{71}Ga and (b) ^{69}Ga. ^{69}Ga, the isotope with the larger quadrupolar moment and smaller magnetic moment, transitions from the (negative) hyperfine regime to the (positive) quadrupolar regime at higher irradiation intensity. (c) Spatial patterns are due to the various "zones" where either the hyperfine or quadrupolar mechanism may dominate. (d) Simulated STRAFI images for ^{69}Ga capture the changing shape of the distribution of nuclear polarization with illumination intensity. For (a) the intensities are (i) 5 mW/cm^2, (ii) 10 mW/cm^2, (iii) 35 mW/cm^2, (iv) 75 mW/cm^2. For both (b) and (d) the intensities are (i) 6 mW/cm^2, (ii) 14 mW/cm^2, (iii) 38 mW/cm^2, (iv) 83 mW/cm^2. (From [21].)

Furthermore, optical pumping can be combined with NMR pulse sequences to further control nuclear polarization. As a proof of principle, we combined periods of optical pumping of varied intensity and wavelength with NMR π pulses to isolate regions of hyperfine- and quadrupolar-induced polarization (Fig. 5.5). Many sophisticated NMR pulse sequences exist that interconvert various types of spin order and coherence, which may be combined with wavelength, intensity, and helicity control of spatially-patterned polarization to create a range of spatially-dependent spin dynamics.

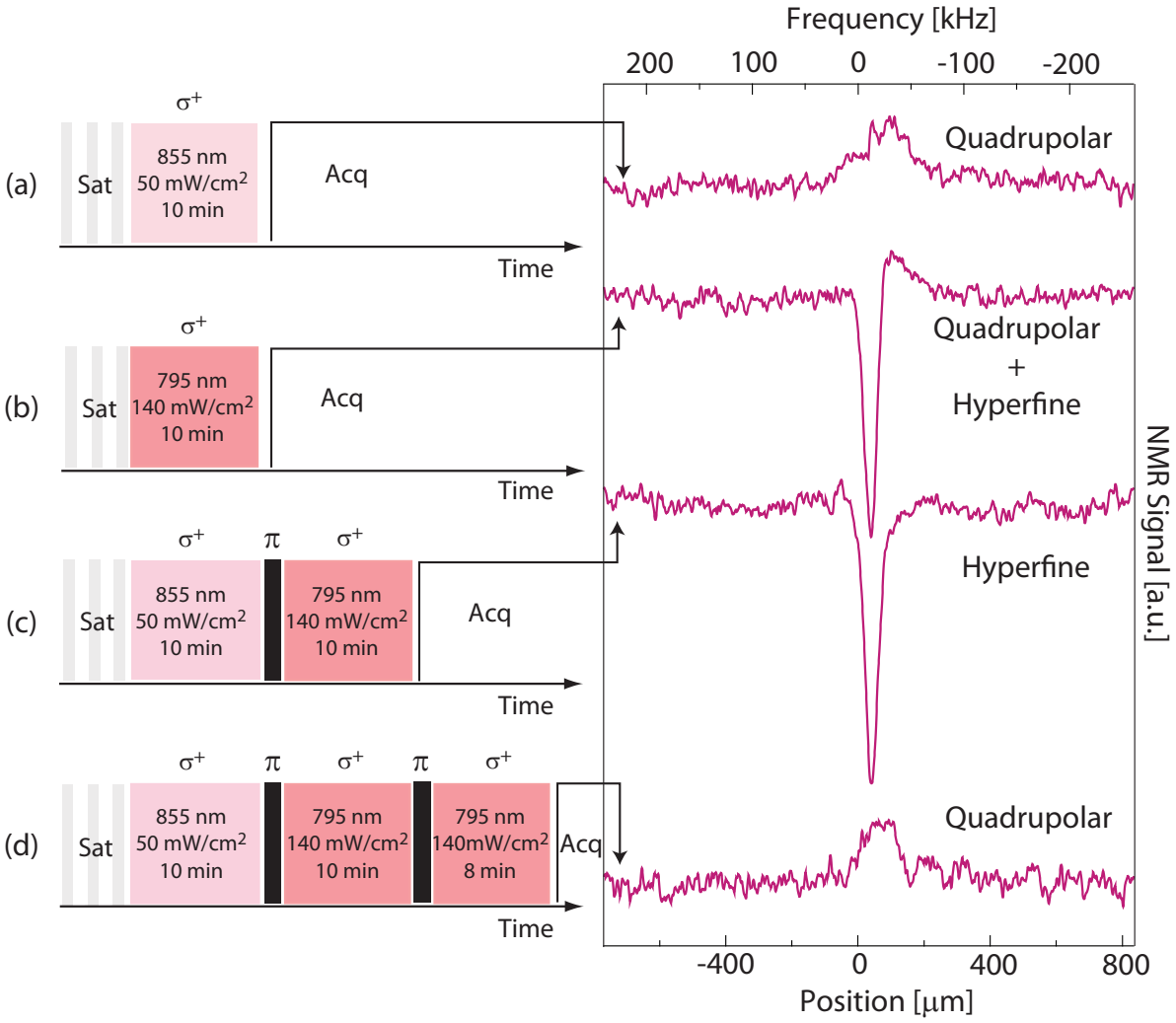

Figure 5.5: Engineering Nuclear Magnetism

Optical pumping parameters may be chosen so that (a) quadrupolar relaxation dominates, or (b) both mechanisms act simultaneously on different regions in the sample. By combining periods of optical pumping with different intensity and wavelength, separated by π pulses, only the (c) hyperfine or (d) quadrupolar polarized regions remain. (From [21].)

5.3 Discussion

We have demonstrated an all-optical method to create patterns of polarized nuclear spins from millimeter to micron length scales. All regimes are easily accessible under typical laboratory conditions. Rastering of the laser beam will provide an additional 2 dimensions of spatial control and combining NMR pulse sequences with optical irradiation gives a general scheme for creating patterns. These patterns persist for a time scale equal to the nuclear spin-lattice relaxation time, minutes to hours under these conditions, which is more than sufficient for any NMR pulse sequence or quantum computing protocol. Patterns may be erased (saturation), reoriented (θ° RF pulses), or converted to various types of spin-order through available NMR pulse sequences. We also note that for applications where the surface depletion layer is undesired, Fermi-level pinning does not occur, for example, on a freshly cleaved (110) GaAs surface[49] and may be avoided with an inert atmosphere or protective encapsulation.

We call specific attention to the possibility of using patterned nuclear polarization to create effective Zeeman fields in electron-spin based devices. Such fields may be used to selectively tune the resonance frequency of confined electrons. Coherent electron spin rotations have already been achieved[30], by causing electrons to drift through a region of magnetized nuclei. Micron-level, 3-dimensional control of nuclear magnetism gives a new degree of freedom in semiconductor spintronics which will be easily integrated into existing device architectures with optical and electrical control.

We also note that the relative rates of the two polarization mechanisms are a function of distance from a given recombination center. This suggests the possibility of achieving patterned polarization on a length scale similar to the Bohr radius ($\sim$10nm in GaAs). For an s-orbital like hydrogenic wavefunction the hyperfine polarization rate is greatest where the electron density is highest (near the recombination center) and becomes small outside the Bohr radius. In contrast, the quadrupolar mechanism relies on fluctuations in the gradient of the electric field. Symmetry considerations dictate that no gradients exist at the center of a spherically symmetric environment, so the behavior near the recombination center is dominated by the hyperfine interaction. The quadrupolar interaction reaches a maximum on the order of the Bohr radius from the defect site and decays less rapidly as a function of distance. Future studies will investigate the local distribution of nuclear polarization near defects.

5.4 Methods

Stray-Field NMR Imaging

NMR images for ^{71}Ga and ^{69}Ga are obtained using the stray field of a 9.4 T superconducting NMR magnet. The RF pulse sequence is SAT-τ_L -$\pi/2$, where SAT is the saturation of the spin transitions by a series of pulses, τ_L is the irradiation time, and the final $\pi/2$-pulse (8

μs) converts the nuclear polarization into observable coherences. The sample is a [100] wafer of semi-insulating GaAs (American Crystal Technologies) with resistivity greater than 10^7 Ωcm. To ensure good thermal conductivity, we use Apiezon N grease to mount the sample of thickness 350 μm atop a long, rectangular sapphire strip. The strip bridges the opposite sides of a $\sim$3 cm diameter opening at the center of a thin copper plate, whose orientation relative to the static magnetic field can be (slightly) adjusted using screws connected to the outside of the cryostat via long G10 rods. A split-coil surrounding the sample (and sapphire wafer) as part of a purpose-made cryogenic probe serves as the radio-frequency source. The coil shape and size are chosen so as to optimize the sample filling-factor while avoiding making physical contact with the support wafer or GaAs crystal. As shown in Fig. 1, the area illuminated by the laser beam on the sample surface is defined by a proximal 1x1 mm^2 square window etched on an aluminum-coated sapphire strip aligned to coincide with the coil central gap. We use an optical expander to widen the laser beam so as to reach a 5-mm-diameter waist before the Al window, thus ensuring homogeneous intensity over the optically pumped surface. We control the beam helicity using a linear polarizer and a quarter wave plate. We illuminate the sample at 6.5 K through the quartz windows at the bottom of a modified Janis-Varitran cryostat, and use the G10 rods protruding at the upper end of our NMR probe to align the GaAs wafer perpendicular to the direction of the static magnetic field. To accomplish this, we adjust the copper plate orientation while monitoring the part of the laser beam reflected from the aluminum-coated sapphire; this method allows us to reach a sample orientation precision better than half a degree. In preparation for the optical-pumping experiments reported herein, we conducted extensive preliminary experiments aimed at determining the magnetic field gradient as a function of the sample position within the magnet bore. For this purpose, we recorded the ^{71}Ga NMR signal from a 350-μm-thick GaAs wafer at room temperature for multiple displacements of the cryostat from its rest position atop the magnet. NMR spectra were attained using a simple excitation-acquisition protocol with 1-μs-long RF pulses so as to ensure the broadest excitation bandwidth possible. The magnetic field gradient is linear over the sample volume and exceeds 70 T/m at the maximum displacements we tested. For the present optical pumping experiments, we use a somewhat moderate gradient ($\sim$19 T/m) as a reasonable tradeoff between spatial resolution and signal-to-noise ratio for typical illumination times ($\sim$10 min). Unless otherwise noted, the illumination wavelength is 825nm.

Chapter 6

Conclusions and Advice for Future Researchers

The two main topics discussed in this dissertation, the polarization of nuclear spins in diamond and gallium arsenide, share some common attributes. In both systems one can readily generate spin-polarized electrons via optical illumination. In gallium arsenide two mechanisms of nuclear polarization are present, a magnetic hyperfine interaction that drives the nuclear spins to a highly polarized non-equilibrium state, and an electric quadrupole interaction that drives the nuclear spins to equilibrium with the lattice temperature. In diamond, we establish a spin temperature in the dipolar energy reservoir formed by many interacting defects. This reservoir is thermally connected to the nuclear spin Zeeman energy and drives the nuclear spins to a highly refrigerated equilibrium state. While we have provided the groundwork for understanding the basic physics, there is still much work to be done to fully understand these systems, especially in the case of diamond. Additionally, there exists the opportunity for exciting new applications of this knowledge. In the following sections I will outline some ideas that future researchers may pursue:

6.1 Orientation Dependence in Diamond

Studies are already under way in the Reimer lab to determine the dependence of the nuclear spin polarization on the orientation of the sample crystal in the magnetic field. These data are still preliminary, but it appears that theoretical descriptions developed in this dissertation are not yet sufficient to capture these phenomena. A full understanding must include the angular dependence of the spin-spin Hamiltonian, how the optical pumping behaves when the defect symmetry axis is not aligned with the magnetic field, and light polarization selection rules for optical transitions. Additionally, many of the assumptions made in our initial attempts to model the system must be reexamined, such as the neglect of Hamiltonian terms that do not commute with the Zeeman term.

6.2 Polarization Transfer from Diamond

It has long been a goal of magnetic resonance researchers to transfer nuclear polarization from a highly polarized substrate to target molecules. There are several possible ways this may be accomplished. The first possibility is to transfer polarization from ^{13}C nuclei in the diamond to external molecules. This could be facilitated by using isotopically enriched samples and allowing spin diffusion to transfer polarization to external carbon nuclei. If it is desired to transfer to another nucleus outside the sample, a double-resonance technique will be needed (such as cross polarization) to overcome the energy mismatch. A perhaps more intriguing possibility is to bypass the carbon nuclei altogether. There is no fundamental reason why only ^{13}C should be polarized by the mechanism described here, it is only required that a nucleus be sufficiently near to the NV- centers in order to interact. It may be possible to optimize diamond samples with NV- centers very close to the surface, such that the electron dipolar field extends to nuclei outside the crystal, directly polarizing them. Simulations suggest that NV- centers must be within approximately 1nm of the surface for such a coupling to occur, so it is not yet clear if this method is feasible.

6.3 3-D Patterning and Spintronics in Gallium Arsenide

The work in this dissertation showed proof of concept that nuclear magnetization may be patterned as a function of depth in bulk gallium arsenide samples by varying illumination conditions and using NMR pulse sequences. It should be possible to extend this work further by developing control of the illumination laser in the x-y plane and creating 3-dimensional patterns of nuclear magnetization. The 1-dimensional imaging technique used here must also be revised to image 3-dimensions. Furthermore, microfabricated devices with electrodes may be fabricated to cause electrons to drift through regions of magnetized nuclei. Optical Faraday rotation spectroscopy may be used to investigate how the magnetized nuclei are controlling the drifting electrons.

Bibliography

[1] A. Abragam. *The Principles of Nuclear Magnetism*. Oxford University Press, 1961.

[2] Bauch E. Ledbetter M. P. Santori C. Fu K.-M. C. Barclay P.E. Beausoleil R.G. Linget H. Roch J.F. Treussart F. Chemerisov S. Gawlik W. Acosta V.M. and D. Budker. "Diamonds with a high density of nitrogen-vacancy centers for magnetometry applications". In: *Phys. Rev. B.* 80.115202 (2009).

[3] G. Balasubramanian et al. In: *Nature* 455.7213 (2008), 648–U46.

[4] Pham L. M. Jarmola A. Budker D. Bar-Gill N. and R. L. Walsworth. In: *arXiv:1211.7094* (2012).

[5] L. Childress et al. In: *Science* 314.5797 (2006), pp. 281–285.

[6] P. Coles and J. Reimer. In: *Phys. Rev. B* 76 (2007), p. 174440.

[7] M. V. G. Dutt et al. In: *Science* 316.5829 (2007), pp. 1312–1316.

[8] J. Fabian et al. In: *Acta Physica Slovaca* 57 (2007), p. 565.

[9] M. R. et. al. Fitzsimmons. In: *Phys. Rev. B.* 76.245301 (2007).

[10] T. Gaebel et al. In: *Nature Physics* 2.6 (2006), pp. 408–413.

[11] Ohki S. Hashi K. Goto A. and T. Shimizu. In: *Nat. Commun.* 2.378 (2011).

[12] R. Hanson, O. Gywat, and D. D. Awschalom. In: *Physical Review B* 74.16 (2006).

[13] R. Hanson et al. In: *Physical Review Letters* 97.8 (2006).

[14] R. Hanson et al. In: *Science* 320.5874 (2008), pp. 352–355.

[15] S. E. Hayes, S. Mui, and K. Ramaswamy. In: *Journal of Chemical Physics* (2008), p. 052203.

[16] M. J. R. Hoch and E. C. Reynhardt. In: *Phys. Rev. B* 37.17 (1988), pp. 9222–9226.

[17] V. Jacques et al. In: *Physical Review Letters* 102.5 (2009).

[18] Acosta V. M. K. Jensen Chemerisov S. Jarmola A. and D. Budker. In: *Phys. Rev. Lett.* 108.197601 (2012).

[19] R. K. et al. Kawakami. In: *Science* 294 (2001), pp. 131–134.

[20] Coles P. J. King J. P. and J. A. Reimer. In: *Phys. Rev. B.* 81.073201 (2010).

[21] Li. Y. Meriles C. A. King J. P. and J. A. Reimer. In: *Nat. Commun.* 3.918 (2012).

[22] King J. P. Peng L. Tamargo M. C. Reimer-J. A. Li Y. and C. A. Meriles. In: *Appl. Phys. Lett.* 98.112101 (2011).

[23] J. R. Maze et al. In: *Nature* 455.7213 (2008), 644–U41.

[24] C. A . Michal and R . Tycko. In: *Phys. Rev. B* 60 (1999), pp. 8672–8679.

[25] C. A. Michal and R. Tycko. In: *Phys. Rev. B.* 60.12 (1999), pp. 8672–8679.

[26] S. Mui, K. Ramaswamy, and S. Hayes. In: *J. Chem. Phys* 128 (2008), p. 052303.

[27] S. Mui et al. In: *Phys. Chem. Chem. Phys* 11 (2009), p. 7031.

[28] Kobayashi Y. Komiyama S. Tsuboi M. Nakajima T. and T . Machida. In: *Phys. Rev. B* 81.085322 (2010).

[29] P. Neumann et al. In: *Science* 320.5881 (2008), pp. 1326–1329.

[30] Fuchs G. D. Mack S. Samarth N. Nowakowski M. E. and D. D. Awschalom. In: *Phys. Rev. Lett* 105.137206 (2010).

[31] D. Paget, T. Amand, and J. P. Korb. In: *Phys. Rev. B* 77 (2008), p. 245201.

[32] D. Paget and P.B. Klein. In: *Physical Review B* 34 (1986), p. 971.

[33] journal = Phys. Rev. B volume = 24 pages = 3776 3793-Year = 1977 . n. . E. Paget D. In: ().

[34] A. Paravastu et al. In: *Phys. Rev. B* 69 (2004), p. 075203.

[35] M. et. al. Poggio. In: *Phys. Rev. Lett* 9.207602 (2003).

[36] J. Reimer. In: *Solid State Nuclear Magnetic Resonance* 37 (2010), p. 3.

[37] E. C. Reynhardt and G. L. High. In: *Journal of Chemical Physics* 109.10 (1998), pp. 4090–4099.

[38] E. C. Reynhardt and G. L. High. In: *Journal of Chemical Physics* 109.10 (1998), pp. 4100–4107.

[39] E. C. Reynhardt and G. L. High. In: *Journal of Chemical Physics* 113.2 (2000), pp. 744–750.

[40] Klug C. A. Miller J. B. Sauer K. L. and J. P. Yesinowski. In: *Phys. Rev. B.* 84.085202 (2011).

[41] Berezovsky J. Kawakami R. K. Gossard A. C. Stephens J. and D. D. Awschalom. In: *Appl. Phys. Lett* 85 (2004), pp. 1184–1186.

[42] J. Stephens et al. In: *Physical Review B* 68 (2003), 041307(R).

[43] J. et. al. Stephens. In: *Phys. Rev. B.* 68.041307(R) (2003).

[44] D. Suter and T. S. Mahesh. In: *The Journal of Chemical Physics* 128 (2008), p. 052206.

[45] S. Takahashi et al. In: *Physical Review Letters* 101.4 (2008).

[46] C. J. Terblanche, E. C. Reynhardt, and J. A. van Wyk. In: *Solid State Nuclear Magnetic Resonance* 20.1-2 (2001), pp. 1–22.

[47] J. Vanhouten, W. T. Wenckebach, and N. J. Poulis. In: *Physica B and C* 92.2 (1977), pp. 210–220.

[48] W.M Witzel and S. Das Sarma. In: *Phys. Rev. B* 74.035322 (2006).

[49] P. Y. Yu and M. Cardona. *Fundamentals of Semiconductors*. Springer-Verlag, Berlin, 2001.

Appendix A

Computer Simulations of Nuclear Polarization in Diamond

The following is the code used to generate the simulations published in **??**. The code runs on Mathematica version 8.0.1.0. Note that the term "Cf2," which corresponds to the zero-field splitting for defects aligned 109.5 degrees from the magnetic field, contains an incorrect term. It should read Cf2= $2 * Pi * hbar * 2.88 * 10^9 * \frac{1}{2}(3\cos^2\theta - 1)$.

"C13 OPNMR in Diamond"

C13 OPNMR in Diamond

" Physical Constants and Properties "

```
ClearAll["Global`*"]

c = 3 * 10^8; (*Meters/Second*)
h = 6.626 × 10^-34; (*Joules*Seconds*)
hbar = h / (2 π);(*Joules*Seconds*)
kb = 1.38 * 10^-23;(*Joules/Kelvin*)
γ13C = 10.705 * 10^6;(*Hz/T from Wikipedia*)
(*γNV=-2.560777*10^5*10^6;(*Hz/T, calculated from Wikipedia*)*)
γNV = 1.76 * 10^11 / 2 / Pi;
NA13C = 0.01108;(*Naural Abundance of Carbon-13: Fraction, not percent*)
Bo = 9.4;(*Tesla*)
ωI = γ13C * Bo * 2 * Pi;(*rad/s*)
μ0 = 4 * Pi * 10^(-7);(*T*m/A, from wikipedia*)
```

" Model Parameters "

```
Nnv = 9.5 * 10^18;(*Concentration of NV- Centers Spins/cm^3,
estimated from Awschalom's quenching decoherence papaer*)
(*Ne=10^20;(*Concentration of all non-pumped paramagnets spins/cm^3,
estimated from Awschalom's quenching decoherence papaer*)*)
(*T1e=.01; (*Electron Spin-
 Lattice Relaxation time.  Assumed constant for all paramagnetic defects, Seconds*)
Pnv=0;(*Polarization of NV- centers into the ms = 0 sublevel*)*)
(*Tc=3.510^(-7);(*Correlation time for flucturations,
seconds Rough Guess for now,~1 Gauss linewidth*)*)
Deff = 6.7 * 10^-19; (*Spin Diffusion Coefficient m^2/s,
taken from table 5 of Terblanche et. al (4.7 Tesla!)*)
P0deg = .998;(*818Population of ms=
 0 state for those defects aligned with the magnetic field*)
P109deg = .998;(*Population of ms=
 0 state for those defects 109.5 degrees off the external magnetic field*)
```

" Calculations "

" Preliminary Calculations "

```
Rnv = 1 / 100 * (3 / (4 * π * Nnv)) ^ (1 / 3);
(*Radius under influence of a single NV- Center, Meters*)
```

" Hamiltonian Matrix Elements "

```
Cf := 2 * Pi * hbar * 2.88 * 10^9;(*Zero Field Splitting the 2Pi converts from Hz to rad/s,
final answer in Joules, for defets aligned with B0*)
Cf2 := 2 * Pi * hbar * 2.88 * 10^9 * 1 / 4 * (3 + (Cos[2 * 109.5 / 360 * 2 * Pi]) ^ 2);
(*Zero Field Splitting the 2Pi converts from Hz to rad/s,
final answer in Joules, for defets 109.5 degrees misaligned with B0*)
```

$$V[r\_] := \text{hbar} * \mu 0 / (4 * \pi) * \text{hbar} * (\gamma \text{NV} * 2 * \text{Pi}) * (\gamma 13\text{C} * 2 * \text{Pi}) / r^3 * (-3 / 2) * \frac{2}{3\pi};$$

```
(*Dipolar transition term for nuclear/electron interaction,
ommitted the phi dependance due to axial symmetry,
also averaged over theta to remove all angular dependence*)
(*Converted gammas to radians by multpplying by 2 Pi 8/20/09*)
```

" Transition Rates "

```
A00m = -hbar * ωI - Sqrt[2 * (Cf + Cf) * hbar * ωI + 3 * (hbar * ωI)^3];
(*One of 2 Roots of the argument of the delta function in Fermi's Golden rule,
i.e. the value of A for which ΔE=0, both zero degrees*)
A00p = -hbar * ωI + Sqrt[2 * (Cf + Cf) * hbar * ωI + 3 * (hbar * ωI)^3];
(*One of 2 Roots of the argument of the delta function in Fermi's Golden rule,
i.e. the value of A for which ΔE=0, both zero degrees*)

A11m = -hbar * ωI - Sqrt[2 * (Cf2 + Cf2) * hbar * ωI + 3 * (hbar * ωI)^3];
(*First root of argument delta function for both 109.5degree non-aligned defects*)

A11p = -hbar * ωI + Sqrt[2 * (Cf2 + Cf2) * hbar * ωI + 3 * (hbar * ωI)^3];
(*Second root of argument delta function for both 109.5degree non-aligned defects*)

A01m = -hbar * ωI - Sqrt[2 * (Cf + Cf2) * hbar * ωI + 3 * (hbar * ωI)^3];
(*First root for combination of 0 degree and 109.5 degree defects*)

A01p = -hbar * ωI + Sqrt[2 * (Cf + Cf2) * hbar * ωI + 3 * (hbar * ωI)^3];
(*Second root for combination of 0 degree and 109.5 degree defects*)

Adp = hbar * ωI;(*CHECK THESE MATRIX ELEMENTS FOR CORRECT LADDER OPERATORS*)
Adm = -hbar * ωI;

b[a_] := -1 / 4 * a * Sqrt[2];
(*Just a relationship between A and B of the "dipolar alphabet"*)


N00[a_] := Sqrt[2 + 1 / 4 * ((-a + 2 * Cf + Sqrt[a^2 + 8 * b[a]^2 - 4 * a * Cf + 4 * Cf^2]) / b[a])^2];
N11[a_] :=
  Sqrt[2 + 1 / 4 * ((-a + 2 * Cf2 + Sqrt[a^2 + 8 * b[a]^2 - 4 * a * Cf + 4 * Cf2^2]) / b[a])^2];
N01[a_] := Sqrt[2 + 1 / 4 * ((-a + (Cf + Cf2) + Sqrt[(a^2) / 2 + (a - (Cf + Cf2))^2]) / b[a])^2];
 (*Normalization constant defined as N_3 in my paper,
the numbers refer to the two possible orientations of the defects*)

α = 1;
β = -1;


Nd1[a_] := Sqrt[1 + α^2];
Nd2[a_] := Sqrt[1 + β^2];

δ = (2 * π^2) / (3 * Sqrt[3]) * (γNV * 2 * Pi)^2 * hbar^2 * Nnv;(*Essentially the dipolar linewidth,*)

g[a_] := δ / ((δ^2 + a^2) * π);
(*Describes fluctuations in NV- Centers due to the dipolar interaction,
Lorentzian as shown in Abragam, this is like the density of states*)


" Transport Model " \n \n(*These are the diagonal elements of the 9x9
    density matrix that were calculated in the paper.  The first two numbers refer
    to the orientation of the defects in the pair (0=0degrees,1=109.5 degrees)
    The third number refers to level 1 and level 3 as defined in the paper*)
```

```
P001 := ((1 - P0deg) / 2)^2;
P003[a_] := 1 / (N00[a])^2 * (2 * ((1 - P0deg) / 2)^2 +
      ((-a + 2 * Cf + Sqrt[a^2 + 8 * b[a]^2 - 4 * a * Cf + 4 * Cf^2]) / (2 * b[a]))^2 * (P0deg)^2);

P111 := ((1 - P109deg) / 2)^2;
P113[a_] := 1 / (N11[a])^2 * (2 * ((1 - P109deg) / 2)^2 +
      ((-a + 2 * Cf2 + Sqrt[1 / 2 * a^2 + (a - Cf2 - Cf2)^2]) / (2 * b[a]))^2 * (P109deg)^2);

P011 := (1 - P0deg) * (1 - P109deg) / 4;
P013[a_] := 1 / (N01[a])^2 * (2 * (1 - P0deg) / 2 * (1 - P109deg) / 2 +
      ((-a + (Cf + Cf2) + Sqrt[1 / 2 * a^2 + (a - Cf - Cf2)^2]) / (2 * b[a]))^2 * P0deg * P109deg);


(*These are the total probabilities for a defect
 pair to be in a state that can participate in the tranition*)
Prob00[a_] := P001 + P003[a];
Prob11[a_] := P111 + P113[a];
Prob01[a_] := P011 + P013[a];

Probd00 = 2 * (1 - P0deg) * (P0deg);
Probd11 = 2 * (1 - P109deg) * (P109deg);


(*These are transition rates (as calculated from Fermi's Golden Rule)
 for each of the 3 possible defect pair orientations 00, 10=01, 11,
and also accounting for the two different values of A that gave roots for
 the argument of the delta function. (m and p, stand for plus and minus)*)
W00m[r_] := Prob00[A00m] * (2 * Pi / hbar * (2 * (Abs[V[r]])^2 / (N00[A00m])^2) * g[A00m]) /
     (1 / 2 + 1 / 4 * (6 * A00m - 2 * (Cf + Cf)) / Sqrt[2 * A00m^2 + (A00m - (Cf + Cf))^2]);
W00p[r_] := Prob00[A00p] * (2 * Pi / hbar * (2 * (Abs[V[r]])^2 / (N00[A00p])^2) * g[A00p]) /
     (1 / 2 + 1 / 4 * (6 * A00p - 2 * (Cf + Cf)) / Sqrt[2 * A00p^2 + (A00p - (Cf + Cf))^2]);
W11m[r_] := Prob11[A11m] * (2 * Pi / hbar * (2 * (Abs[V[r]])^2 / (N11[A11m])^2) * g[A11m]) /
     (1 / 2 + 1 / 4 * (6 * A11m - 2 * (Cf2 + Cf2)) / Sqrt[2 * A11m^2 + (A11m - (Cf2 + Cf2))^2]);
W11p[r_] := Prob11[A11p] * (2 * Pi / hbar * (2 * (Abs[V[r]])^2 / (N11[A11p])^2) * g[A11p]) /
     (1 / 2 + 1 / 4 * (6 * A11p - 2 * (Cf2 + Cf2)) / Sqrt[2 * A11p^2 + (A11p - (Cf2 + Cf2))^2]);
W01m[r_] := Prob01[A01m] * (2 * Pi / hbar * (2 * (Abs[V[r]])^2 / (N01[A01m])^2) * g[A01m]) /
     (1 / 2 + 1 / 4 * (6 * A01m - 2 * (Cf + Cf2)) / Sqrt[2 * A01m^2 + (A01m - (Cf + Cf2))^2]);
W01p[r_] := Prob01[A01p] * (2 * Pi / hbar * (2 * (Abs[V[r]])^2 / (N01[A01p])^2) * g[A01p]) /
     (1 / 2 + 1 / 4 * (6 * A01p - 2 * (Cf + Cf2)) / Sqrt[2 * A01p^2 + (A01p - (Cf + Cf2))^2]);
W00dp[r_] := Probd00 * (2 * Pi / hbar * ((Abs[V[r]] * Nd2[Adp] / (Nd1[Adp]^2 * β))^2) * g[Adp]);
W00dm[r_] := Probd00 * (2 * Pi / hbar * ((Abs[V[r]] * Nd2[Adm] / (Nd1[Adm]^2 * β))^2) * g[Adm]);
W11dp[r_] := Probd11 * (2 * Pi / hbar * ((Abs[V[r]] * Nd2[Adp] / (Nd1[Adp]^2 * β))^2) * g[Adp]);
W11dm[r_] := Probd11 * (2 * Pi / hbar * ((Abs[V[r]] * Nd2[Adm] / (Nd1[Adm]^2 * β))^2) * g[Adm]);
W01d[r_] := 0;

(*These are the actual equilibrium polarizations of the dipolar levels of defect pairs
 for each of the 3 orientations and 2 possible values of A per orientation.  A
 weighted combination of these values (weighted by both abundance and transition rate)
 will give the final nuclear polarization*)
Mo00m = (P003[A00m] - P001) / (P003[A00m] + P001);
Mo00p = (P003[A00p] - P001) / (P003[A00p] + P001);
Mo11m = (P113[A11m] - P111) / (P113[A11m] + P111);
Mo11p = (P113[A11p] - P111) / (P113[A11p] + P111);
Mo01m = (P013[A01m] - P011) / (P013[A01m] + P011);
Mo01p = (P013[A01p] - P011) / (P013[A01p] + P011);
```

" Time Evolution of the Spatial Profile of Nuclear Polarization "

```
(*This solves the differential equation for the time
 evolution of direct polarization and spin diffusion in the continuum
 approximation with angular dependence removed by averaging.  *)
solution = NDSolve[{D[M[t, r], t] == Deff * 1 / r^2 * D[r^2 D[M[t, r], r], r] +
       1 / 16 * ((W00m[r] * (Mo00m - M[t, r]) + W00p[r] * (Mo00p - M[t, r])) +
          6 * (W01m[r] * (Mo01m - M[t, r]) + W01p[r] * (Mo01p - M[t, r])) +
          9 * (W11m[r] * (Mo11m - M[t, r]) + W11p[r] * (Mo11p - M[t, r])) - W00dp[r] * M[t, r] -
          W00dm[r] * M[t, r] - 9 * W11dp[r] * M[t, r] - 9 * W11dm[r] * M[t, r]), M[0, r] == 0,
    Derivative[0, 1][M][t, 10^(-12)] == 0, Derivative[0, 1][M][t, Rnv] == 0},
   M, {t, 0, 30 * 60}, {r, 10^(-12), Rnv}];

(*Shows the spatial distribution (with respect to r)
 of the nuclear polarization due to a polarizing defect*)
Plot3D[Evaluate[M[t, r] /. %], {t, 0, 300}, {r, 10^(-11), Rnv},
 PlotRange → All, AxesLabel → {Style["Time (Seconds)", Medium, Bold, Black],
   Style["r (meters)", Medium, Bold, Black], Style["Polarization", Medium, Bold, Black]}]
```

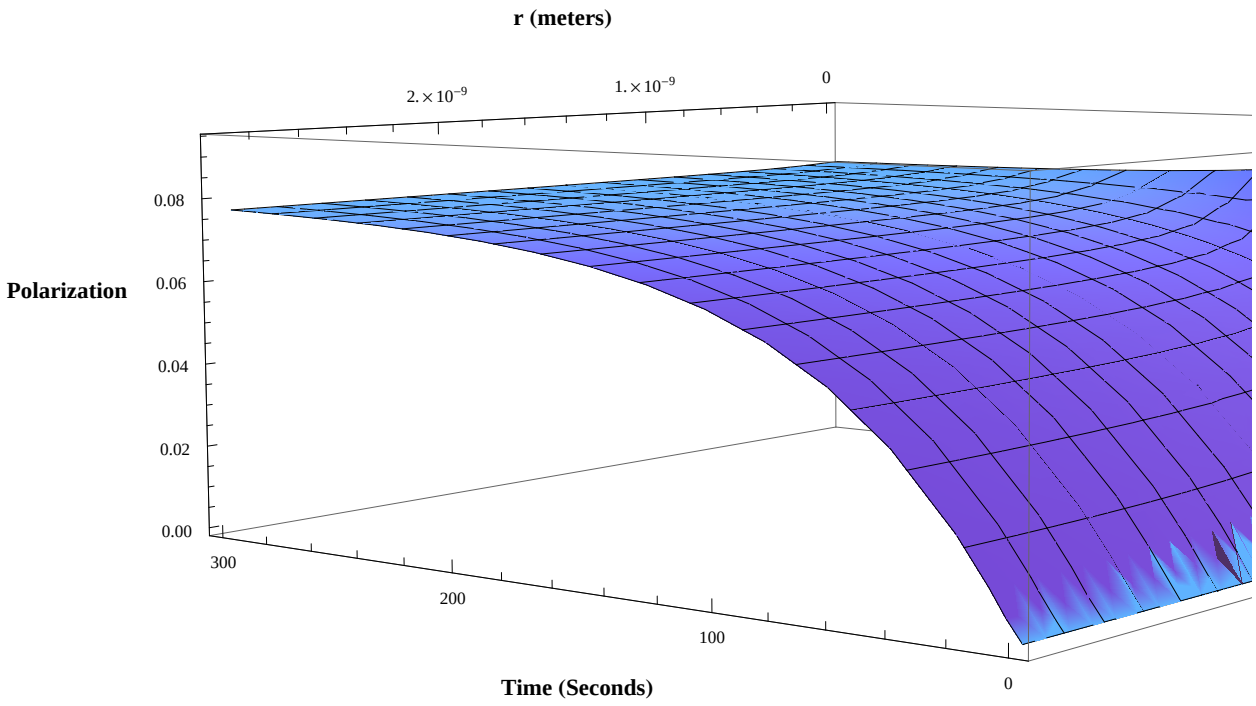

" Prediction for Time Evolution of NMR Signal "

```
Iz[t_] := NIntegrate[Evaluate[(r * 10^9)^2 * M[t, r] /. solution], {r, 10^(-10), Rnv}] /
    (Rnv - 10^(-10)); (*This integration yields the
 bulk averaged nuclear polarization as a function of time*)
```

```
(*Shows rescaled model vs. rescaled data*)
```

Appendix B

Computer Simulations of Patterns of Nuclear Magnetization in Gallium Arsenide

The following is the code used to generate the simulations published in **??**. The code runs on Mathematica version 8.0.1.0.

```
ClearAll["Global`*"]
```

(*Constants*)

```
h = 6.626 × 10^-34;(*Planck's Constant, J*s *)
hbar = h / (2 * Pi);(*Reduced Planck's Constant*)
kb = 1.38 * 10^-23;(*Boltzmann Constant, J/K*)
ec = 1.602 * 10^-19;(*fundamental charge, Coulombs*)
c = 3 * 10^8;(*Speed of Light m/s*)
me = 9.11 * 10^-31;(*Electron Mass, kg*)
β = h * ec / (2 * me * 2 π);(*Bohr Magneton*)
```

(*Model Parameters*)

```
f71 = 2.5 * 10^-14;(*Fitting Parameter in Model*)
f69 = 1.3 * 10^-14;
T = 6.5;(*Temperature in Kelvin*)
τ = 600;(*Masurement time in Arbitrary Units*)
intensity = 40;(*Enter Intensity, mW/cm^2*)
wavelength = 825;(*Enter Laser Wavelength, nm*)
δ = 50 * 10^-6;(*Depletion Layer Thickness*)

B0 = 9.4;(*External Magnetic Field, Tesla*)
γ71 = 121.927 * 10^6 / 9.4 * 2 * Pi;(*Gyromagnetic Ratios Rad/S/Tesla*)
γ69 = 95.993 * 10^6 / 9.4 * 2 * Pi;
γ75 = 68.483 * 10^6 / 9.4 * 2 * Pi;
gGaAs = -0.44;(*is this the free electron g-factor? Do we need both g-factors?*)
ωH = gGaAs * β * B0 / hbar;
σe = 9 * 10^(-16);(*Spin Exchange Cross Section in m^2, from Paget*)
v = .64 * 10^5;(*Electron velocity in m/s, at 6K from Bimberg*)
be = 1.5 * 10^(-3);(*Hyperfine field at the Bohr Radius (Tesla), from Paget*)
a0 = 10^-8;(*Bohr radius, meters, from Wikipedia*)
S0 = -1 / 4;(*Initial Value of <Sz>
 for Photoexcited Electrons for sigma minus irradiation, units of hbar*)
S0m = +1 / 4;(*Initial Value of <Sz>
 for Photoexcited Electrons for sigma minus irradiation, units of hbar*)
k = 1 * 10^-16;(*recombination rate constant (m^3/s)*)
Na = 5 * 10^22;(*Acceptor Concentration, m^-3*)
Nd = 10^22;(*Donor Concentration, m^-3*)
(*vσc=10^(-13);(*Electron capture rate (m^3/s)*)*)
RGa = 2.8 * 10^12;(*Antishielding tensor component, m^-1*)
RAs = 3.2 * 10^12;(*Antishielding tensor component, m^-1*)
Q71 = .106 * 10^(-28);(*Quadrupole Moment, m^2*)
(*.107*10^(-28);,.19*10^(-28);,.29*10^(-28);*)
Q69 = .168 * 10^(-28);(*Quadrupole Moment, m^2*)
(*Modified these while fitting, need to change to Correct Values!!!*)
Q75 = .315 * 10^(-28);(*Quadrupole Moment, m^2*)
ϵ = 8.854 * 10^(-12);(*Vacuum Permittivity, Coulombs/(V*m)*)
ϵ0 = 12.9;(*Relative permittivity*)
σc = 5.1 * 10^-19;(*Cross Section for electron capture at shallow donors m^2*)
C2 = k / (σc * v * Nd)^2;
```

(*Absorption Data near the Band Gap Energy (The Compillation of absorption data was done by Pat Coles*)

```
absdata = {{0, 0} {1.48755`, 10}, {1.48895`, 11}, {1.48915`, 11}, {1.4899499999999999`, 12},
   {1.4900499999999999`, 12}, {1.49065`, 13}, {1.49155`, 14}, {1.49175`, 14.5`},
   {1.4922499999999999`, 15.4`}, {1.49275`, 17.5`}, {1.49305`, 18},
   {1.49365`, 20}, {1.49395`, 20}, {1.49475`, 22}, {1.49545`, 22}, {1.49565`, 25},
   {1.49655`, 27}, {1.4966`, 30.5`}, {1.49755`, 35}, {1.4981499999999999`, 40.5`},
   {1.49905`, 45}, {1.49985`, 49}, {1.5004499999999998`, 54}, {1.50155`, 60},
   {1.5023499999999999`, 64}, {1.50345`, 70}, {1.5040499999999999`, 76},
   {1.50545`, 82}, {1.5063499999999999`, 95}, {1.50675`, 119}, {1.50685`, 160.`},
   {1.50775`, 220.00000000000003`}, {1.5085499999999998`, 300},
   {1.509`, 409.99999999999994`}, {1.5092999999999999`, 500}, {1.50965`, 610.`},
   {1.5101499999999999`, 790.`}, {1.5104499999999998`, 1000}, {1.51085`, 1100.`},
   {1.51155`, 1550.`}, {1.51185`, 1750.`}, {1.5125`, 3880.`}, {1.51375`, 23920.`},
   {1.515`, 5240.`}, {1.5162499999999999`, 4800.`}, {1.5174999999999998`, 5400.`},
   {1.5187499999999998`, 6320.`}, {1.5199999999999998`, 7480.`},
   {1.52125`, 11399.999999999998`}, {1.5225`, 11000.`}, {1.52375`, 10000.`},
   {1.525`, 10280.`}, {1.5262499999999999`, 11960.`}, {1.5274999999999999`, 17000.`},
   {1.5287499999999998`, 13600.000000000002`}, {1.5299999999999998`, 10600.`},
   {1.53125`, 9520.`}, {1.5325`, 10600.`}, {1.53375`, 11500.`},
   {1.535`, 12240.`}, {1.53625`, 13000.`}, {1.5374999999999999`, 13200.`},
   {1.5387499999999998`, 13200.`}, {1.5399999999999998`, 15640.`},
   {1.5412499999999998`, 14400.`}, {1.5425`, 12360.`}, {1.54375`, 13000.`},
   {1.545`, 14360.`}, {1.54625`, 13360.`}, {1.5474999999999999`, 13180.`},
   {1.5487499999999998`, 13680.000000000002`}, {1.5499999999999998`, 14240.`},
   {1.5512499999999998`, 15600.`}, {1.5525`, 18460.`}, {1.55375`, 14200.`},
   {1.555`, 12960.`}, {1.55625`, 13600.000000000002`}, {1.5574999999999999`, 14120.`},
   {1.5587499999999999`, 14440.`}, {1.5599999999999998`, 14840.`}};
  (*Did some "doctoring" of these data to remove points with the
  same energy and also added in the first point
  to make extrapolation not go negative*)
abs = Interpolation[absdata, InterpolationOrder → 2];


Show[ListPlot[absdata, PlotRange → {{1.49, 1.56}, {0, 29 000}}],
  Plot[abs[e], {e, 1.49, 1.56}, PlotRange → {{1.49, 1.56}, {0, 29 000}}]]
  (*This plots the compiled data points for optical obsorption with
  the interpolation function used in the model superimposed on top*)
```

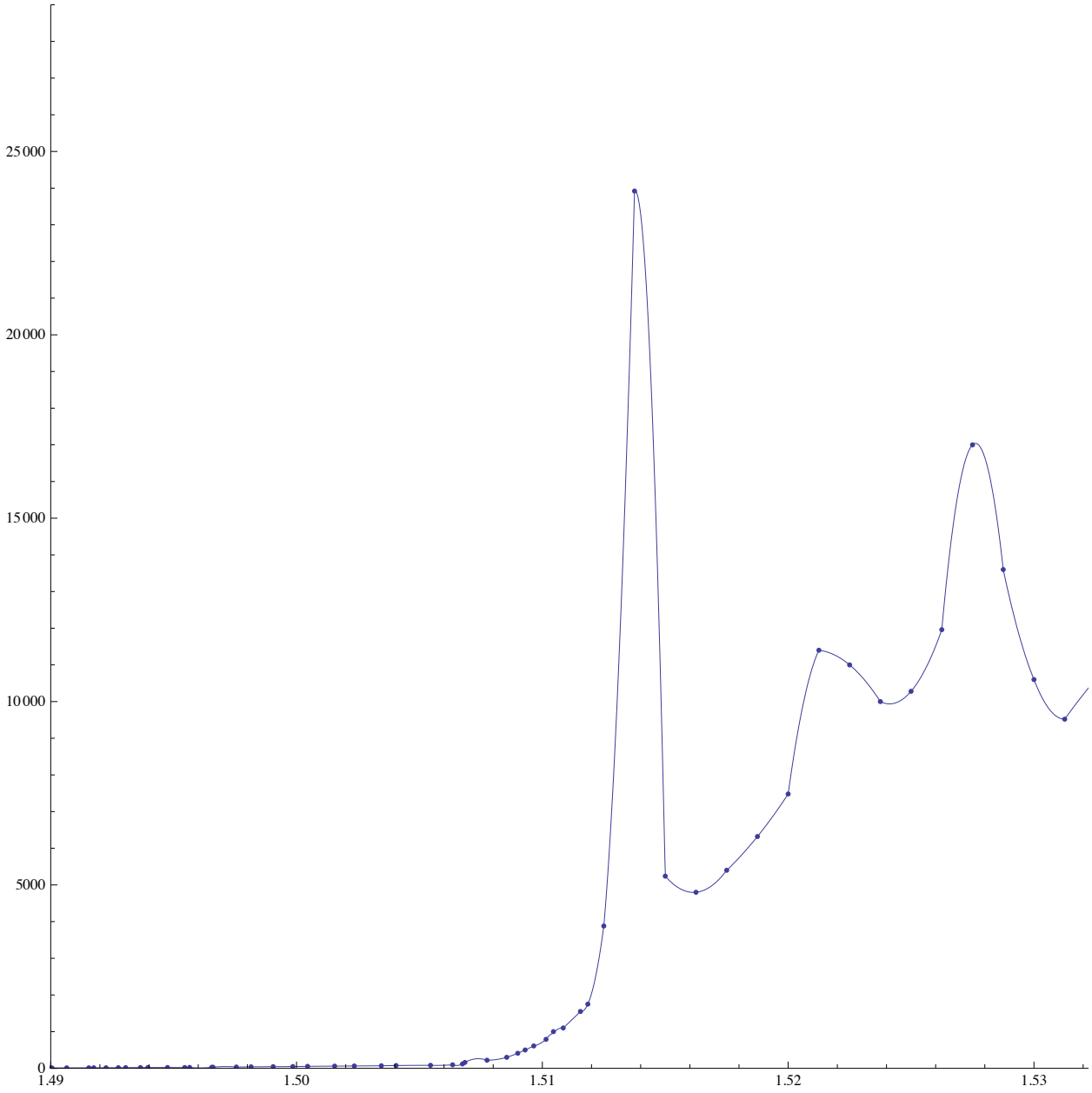


```
(*Show[ListPlot[DataCombinedLT],Plot[10*Exp[((x-1.485)/.0125)^2.1],{x,1.48,1.495}]]*)
```

(*Equations for free electron concentration and donor occupation fraction adapted from Pat Coles*)

```
α[E0_] := abs[E0] * 100;(*Absorption coefficients, conveted to m^-1*)
G[z_, E0_, P_] = P / 1000 * 10^4 * Exp[-α[E0] * z] * α[E0] / E0 / (1.60217646 * 10^(-19));
(*Electron generation rate m^-3s^-1, includes conversion to mW/cm^2 and eV to Joules*)
(*I changed some things from the original version here, make sure its correct*)
ns[z_, E0_, P_] := (G[z, E0, P] / k)^.5;
(*Free electron concentration  based on simple bimolecular recombination model*)
(*Γ[z_,E0_,P_]:=ns[z,E0,P]/(ns[z,E0,P]+Nd*σc*v/(2*k))+10^-10;*)
Γ[z_, E0_, P_] := UnitStep[z - δ] * ns[z, E0, P] / (ns[z, E0, P] + Nd * σc * v / (2 * k)) + 10^-10;
(*Donor occupation fraction based on Langmurian binding behavior*)


Seq = 0.5 * Tanh[-gGaAs * β * 9.4 / (2 * kb * T)];
(*Themal equilibrium value for Sz for electronscheck sign on this*)
ΔS[z_, E0_, P_] = (S0 - Seq) / (1 + (4 / (1 + √(4 G[z, E0, P] * C2 + 1)))); (*The steady-
 state departure of electron polarization from its equilibrium value for sigma+*)
ΔSm[z_, E0_, P_] = (S0m - Seq) / (1 + (4 / (1 + √(4 G[z, E0, P] * C2 + 1)))); (*The steady-
 state departure of electron polarization from its equilibrium value for sigma-*)
(*Sz[z_,E0_,P_]=(S0+Seq*2/(√(4 G[z,E0,P]*C2+1 )+1))/C3))/
   (1+2/(√(4 G[z,E0,P]*C2+1 )+1))/C3);
Te[z_,E0_,P_]=-gGaAs*β*9.4/(2*kb*ArcTanh[2*ΔS[z,E0,P]]);*)
Ih71[z_, E0_, P_] = 5 * ΔS[z, E0, P];(*The steady-
 state nuclear polarizations under the sole effect of hyperfine DNP, sigma+*)
Ih69[z_, E0_, P_] = 5 * ΔS[z, E0, P];
Ih75[z_, E0_, P_] = 5 * ΔS[z, E0, P];
Ih71m[z_, E0_, P_] = 5 * ΔSm[z, E0, P];(*The steady-
 state nuclear polarizations under the sole effect of hyperfine DNP, sigma-*)
Ih69m[z_, E0_, P_] = 5 * ΔSm[z, E0, P];
Ih75m[z_, E0_, P_] = 5 * ΔSm[z, E0, P];
Iq71 = 1 / 2 * Tanh[9.4 * γ71 * hbar / (2 * kb * T)] + Tanh[9.4 * γ71 * hbar / (kb * T)];
(*The equilibrium polarizations under the sole effect of quadrupolar relaxation*)
Iq69 = 1 / 2 * Tanh[9.4 * γ69 * hbar / (2 * kb * T)] + Tanh[9.4 * γ69 * hbar / (kb * T)];
Iq75 = 1 / 2 * Tanh[9.4 * γ75 * hbar / (2 * kb * T)] + Tanh[9.4 * γ75 * hbar / (kb * T)];

!²
```

(*Solutions for sigma+ polarization*)

```
AB71[z_, E0_, P_] = (Γ[z, E0, P]) / (1 - Γ[z, E0, P]) * (γ71^2 / (RGa^2 * Q71^2)) * f71;
(*The Factor A divided by B in my notes*)
D71[z_, E0_, P_] = a0^3 * 4 * Pi * Nd * γ71^2 * be^2 * Exp[4] *
    Γ[z, E0, P] / (ωH^2 / (σe * v * ns[z, E0, P]));(*The Factor D in my notes*)
E71[z_, E0_, P_] = 1 / 32 + 5 / (8 * AB71[z, E0, P] * a0^4);(*The Factor E in my notes*)
F71[z_, E0_, P_] = Ih71[z, E0, P] / 32 + 5 / 8 * Iq71 / a0^4 / AB71[z, E0, P];
(*The Factor F in my notes*)

AB69[z_, E0_, P_] = (Γ[z, E0, P]) / (1 - Γ[z, E0, P]) * (γ69^2 / (RGa^2 * Q69^2)) * f69;
D69[z_, E0_, P_] =
  a0^3 * 4 * Pi * Nd * γ69^2 * be^2 * Exp[4] * Γ[z, E0, P] / (ωH^2 / (σe * v * ns[z, E0, P]));
E69[z_, E0_, P_] = 1 / 32 + 5 / (8 * AB69[z, E0, P] * a0^4);
F69[z_, E0_, P_] = Ih69[z, E0, P] / 32 + 5 / 8 * Iq69 / a0^4 / AB69[z, E0, P];

AB75[z_, E0_, P_] = (Γ[z, E0, P]) / (1 - Γ[z, E0, P]) * (γ75^2 / (RAs^2 * Q75^2)) * f75;
D75[z_, E0_, P_] =
  a0^3 * 4 * Pi * Nd * γ75^2 * be^2 * Exp[4] * Γ[z, E0, P] / (ωH^2 / (σe * v * ns[z, E0, P]));
E75[z_, E0_, P_] = 1 / 32 + 5 / (8 * AB75[z, E0, P] * a0^4);
F75[z_, E0_, P_] = Ih75[z, E0, P] / 32 + 5 / 8 * Iq75 / a0^4 / AB75[z, E0, P];


Iz71[z_, E0_, P_] := F71[z, E0, P] / E71[z, E0, P] * (1 - Exp[-D71[z, E0, P] * E71[z, E0, P] * τ]);
(*The analytical solution for Iz in the fast diffusion, high-field limit*)
Iz69[z_, E0_, P_] := F69[z, E0, P] / E69[z, E0, P] * (1 - Exp[-D69[z, E0, P] * E69[z, E0, P] * τ]);
Iz75[z_, E0_, P_] := F75[z, E0, P] / E75[z, E0, P] * (1 - Exp[-D75[z, E0, P] * E75[z, E0, P] * τ]);
```

(*Solutions for sigma− polarization*)

```
AB71m[z_, E0_, P_] = (Γ[z, E0, P]) / (1 - Γ[z, E0, P]) * (γ71^2 / (RGa^2 * Q71^2)) * f71;
D71m[z_, E0_, P_] =
  a0^3 * 4 * Pi * Nd * γ71^2 * be^2 * Exp[4] * Γ[z, E0, P] / (ωH^2 / (σe * v * ns[z, E0, P]));
E71m[z_, E0_, P_] = 1 / 32 + 5 / (8 * AB71m[z, E0, P] * a0^4);
F71m[z_, E0_, P_] = Ih71m[z, E0, P] / 32 + 5 / 8 * Iq71 / a0^4 / AB71m[z, E0, P];

AB69m[z_, E0_, P_] = (Γ[z, E0, P]) / (1 - Γ[z, E0, P]) * (γ69^2 / (RGa^2 * Q69^2)) * f69;
D69m[z_, E0_, P_] =
  a0^3 * 4 * Pi * Nd * γ69^2 * be^2 * Exp[4] * Γ[z, E0, P] / (ωH^2 / (σe * v * ns[z, E0, P]));
E69m[z_, E0_, P_] = 1 / 32 + 5 / (8 * AB69m[z, E0, P] * a0^4);
F69m[z_, E0_, P_] = Ih69m[z, E0, P] / 32 + 5 / 8 * Iq69 / a0^4 / AB69m[z, E0, P];

AB75m[z_, E0_, P_] = (Γ[z, E0, P]) / (1 - Γ[z, E0, P]) * (γ75^2 / (RAs^2 * Q75^2)) * f00;
D75m[z_, E0_, P_] =
  a0^3 * 4 * Pi * Nd * γ75^2 * be^2 * Exp[4] * Γ[z, E0, P] / (ωH^2 / (σe * v * ns[z, E0, P]));
E75m[z_, E0_, P_] = 1 / 32 + 5 / (8 * AB75m[z, E0, P] * a0^4);
F75m[z_, E0_, P_] = Ih75m[z, E0, P] / 32 + 5 / 8 * Iq75 / a0^4 / AB75m[z, E0, P];


Iz71m[z_, E0_, P_] :=
  F71m[z, E0, P] / E71m[z, E0, P] * (1 - Exp[-D71m[z, E0, P] * E71m[z, E0, P] * τ]);
Iz69m[z_, E0_, P_] := F69m[z, E0, P] / E69m[z, E0, P] *
    (1 - Exp[-D69m[z, E0, P] * E69m[z, E0, P] * τ]);
Iz75m[z_, E0_, P_] := F75m[z, E0, P] / E75m[z, E0, P] *
    (1 - Exp[-D75m[z, E0, P] * E75m[z, E0, P] * τ]);
(*ListPlot[Table[{Energy,Sum[Iz71[z,Energy,50],{z,0,.35*10^-3,10^-7}]},
  {Energy,1.48,1.55,.0001}],PlotJoined→True,PlotRange→All]*)
```

(*This plot reproduces the photon energy spectrum for OPNMR for a given power and helicity*)

**(*This simulates bulk OPNMR data as a function of laser intenisty with
experimental points displayed, done by summing Iz over the depth of the sample*)**

```
(*Show[
 ListPlot[{Table[{P,10^7*Sum[Iz71[z,1.503,P],{z,0,.35*10^-3,.00001}]},{P,0,15,.1}],
   Table[{P,10^7*Sum[Iz71m[z,1.503,P],{z,0,.35*10^-3,.00001}]},{P,0,15,.1}]
   (*,Table[{P,10^6*Sum[Iz69[z,1.503,P],{z,0,.35*10^-3,.00001}]},{P,0,20,.1}],
   Table[{P,10^6*Sum[Iz75[z,1.503,P],{z,0,.35*10^-3,.00001}]},{P,0,20,.1}]*)},
  AxesStyle→Thick,TicksStyle→Thick,PlotStyle→{Thickness[.005]},LabelStyle→(FontSize→42),
  AxesLabel→{Style["",Large,Bold,Black],Style["",Large,Bold,Black]},
  PlotRange→{{0,10},{-25,50}},PlotJoined→True],
 ListPlot[{{{22.2,-61.508},{12.8,-39.679},{7.99,-22.295},{4.21,-7.908},
    {3.03,-3.836},{2.02,-1.294},{1.53,2.603},{1.02,3.66},{0.802,3.998},
    {0.623,4.254},{0.44,4.178},{0.197,4.249},{0.118,3.646},{0.086,3.605},
    {0.0535,3.068},{0.0244,2.916},{0.0104,2.568},{0,1.058}}(*,
   {{13.5,2*-6.076},{8,2*-2.749},{6.06,2*-1.33},{5.14,2*-1.021},{4,2*0.654},
    {3,2*1.172},{2.06,2*1.708},{1.34,2*1.955},{1.06,2*2.116},{0.87,2*1.989},
    {0.658,1.965},{0.36,2.093},{0.246,1.643},{0.101,1.78},{0.068,1.6},
    {0.035,1.512},{0.013,1.224},{0,0.603}},{{22.4,.25*-12.737},{21,.25*-10.517},
    {15.5,.25*-9.515},{12.7,.25*-7.039},{10.3,.25*-4.945},{8.18,.25*5.625},
    {5.4,.25*8.992},{1.98,.25*10.236},{1.05,.25*11.167},{0.82,.25*10.561},
    {0.55,.25*10.439},{0.267,.25*9.222},{0.101,.25*8.993},{0.079,.25*7.558},
    {0.038,.25*6.906},{0.016,.25*5.516},{0.008,.25*3.794},{0,.25*1.765}}*)},
  PlotMarkers→{Automatic,30},PlotRange→{{0,25},{-25,5}}]]
```

```
(*Plot[{Iz71[z/10^6,1.503,1]},{z,0,350},PlotRange→All,
 AxesLabel→{Style["  Depth, μm",(FontSize→36),Bold,Black],
   Style["<Iz>, Arb. Units",(FontSize→36),Bold,Black]},
 LabelStyle→(FontSize→36),PlotStyle→{Thick,Black}]*)
```

STRAFI Simulations

Simulations STRAFI

```
Δ = 4;(*Natural Linewidth in KHz*)
grad = 19;(*Linear gradient in T/m*)
```

```
(*Images are simulated by convoluting the profile of Iz with a Lorentzian lineshape*)

(*image1[ν_]:=
 10^15*NIntegrate[Iz71[z,1.503,2/(.25*.25*Pi)]/(1+((ν-z*grad*γ71/(2*Pi)/1000)/Δ)^2),
   {z,0,350*10^-6}];image2[ν_]:=10^15*NIntegrate[
   Iz71[z,1.503,4/(.25*.25*Pi)]/(1+((ν-z*grad*γ71/(2*Pi)/1000)/Δ)^2),{z,0,350*10^-6}];
image3[ν_]:=10^15*NIntegrate[Iz71[z,1.503,14/(.25*.25*Pi)]/
    (1+((ν-z*grad*γ71/(2*Pi)/1000)/Δ)^2),{z,0,350*10^-6}];
image4[ν_]:=10^15*NIntegrate[Iz71[z,1.503,30/(.25*.25*Pi)]/
    (1+((ν-z*grad*γ71/(2*Pi)/1000)/Δ)^2),{z,0,350*10^-6}];*)
image5[ν_] := 10^15 * NIntegrate[Iz69[z, 1.503, 2 / (.25 * .25 * Pi)] /
     (1 + ((ν - z * grad * γ71 / (2 * Pi) / 1000) / Δ)^2), {z, 0, 350 * 10^-6}];
image6[ν_] := 10^15 * NIntegrate[Iz69[z, 1.503, 5 / (.25 * .25 * Pi)] /
     (1 + ((ν - z * grad * γ71 / (2 * Pi) / 1000) / Δ)^2), {z, 0, 350 * 10^-6}];
image7[ν_] := 10^15 * NIntegrate[Iz69[z, 1.503, 14 / (.25 * .25 * Pi)] /
     (1 + ((ν - z * grad * γ71 / (2 * Pi) / 1000) / Δ)^2), {z, 0, 350 * 10^-6}];
image8[ν_] := 10^15 * NIntegrate[Iz69[z, 1.503, 30 / (.25 * .25 * Pi)] /
     (1 + ((ν - z * grad * γ71 / (2 * Pi) / 1000) / Δ)^2), {z, 0, 350 * 10^-6}];
```

This series ofplots simulates the power dependence of STRAFI data

```
(*Plot[{image1[ν+70]},{ν,-200,200}, PlotRange→All,Axes→{True,False},AxesStyle→Thick,
  TicksStyle→Thick,AxesLabel→{Style["  kHz",(FontSize→42),Bold,Black]},
  LabelStyle→(FontSize→42),PlotStyle→{Thickness[.005]}]
 Plot[{image2[ν+70]},{ν,-200,200}, PlotRange→All,Axes→{True,False},AxesStyle→Thick,
  TicksStyle→Thick,AxesLabel→{Style["  kHz",(FontSize→42),Bold,Black]},
  LabelStyle→(FontSize→42),PlotStyle→{Thickness[.005]}]
 Plot[{image3[ν+70]},{ν,-200,200}, PlotRange→All,Axes→{True,False},AxesStyle→Thick,
  TicksStyle→Thick,AxesLabel→{Style["  kHz",(FontSize→42),Bold,Black]},
  LabelStyle→(FontSize→42),PlotStyle→{Thickness[.005]}]
 Plot[{image4[ν+70]},{ν,-200,200}, PlotRange→All,Axes→{True,False},AxesStyle→Thick,
  TicksStyle→Thick,AxesLabel→{Style["  kHz",(FontSize→42),Bold,Black]},
  LabelStyle→(FontSize→42),PlotStyle→{Thickness[.005]}]*)
Plot[{image5[ν + 70]}, {ν, -200, 200}, PlotRange → All,
 Axes → {True, False}, AxesStyle → Thick, TicksStyle → Thick,
 AxesLabel → {Style["  kHz", (FontSize → 42), Bold, Black]},
 LabelStyle → (FontSize → 42), PlotStyle → {Thickness[.005]}]
Plot[{image6[ν + 70]}, {ν, -200, 200}, PlotRange → All,
 Axes → {True, False}, AxesStyle → Thick, TicksStyle → Thick,
 AxesLabel → {Style["  kHz", (FontSize → 42), Bold, Black]},
 LabelStyle → (FontSize → 42), PlotStyle → {Thickness[.005]}]
Plot[{image7[ν + 70]}, {ν, -200, 200}, PlotRange → All,
 Axes → {True, False}, AxesStyle → Thick, TicksStyle → Thick,
 AxesLabel → {Style["  kHz", (FontSize → 42), Bold, Black]},
 LabelStyle → (FontSize → 42), PlotStyle → {Thickness[.005]}]
Plot[{image8[ν + 70]}, {ν, -200, 200}, PlotRange → All,
 Axes → {True, False}, AxesStyle → Thick, TicksStyle → Thick,
 AxesLabel → {Style["  kHz", (FontSize → 42), Bold, Black]},
 LabelStyle → (FontSize → 42), PlotStyle → {Thickness[.005]}]
```

data dependence of ofplots power series simulates STRAFI the This

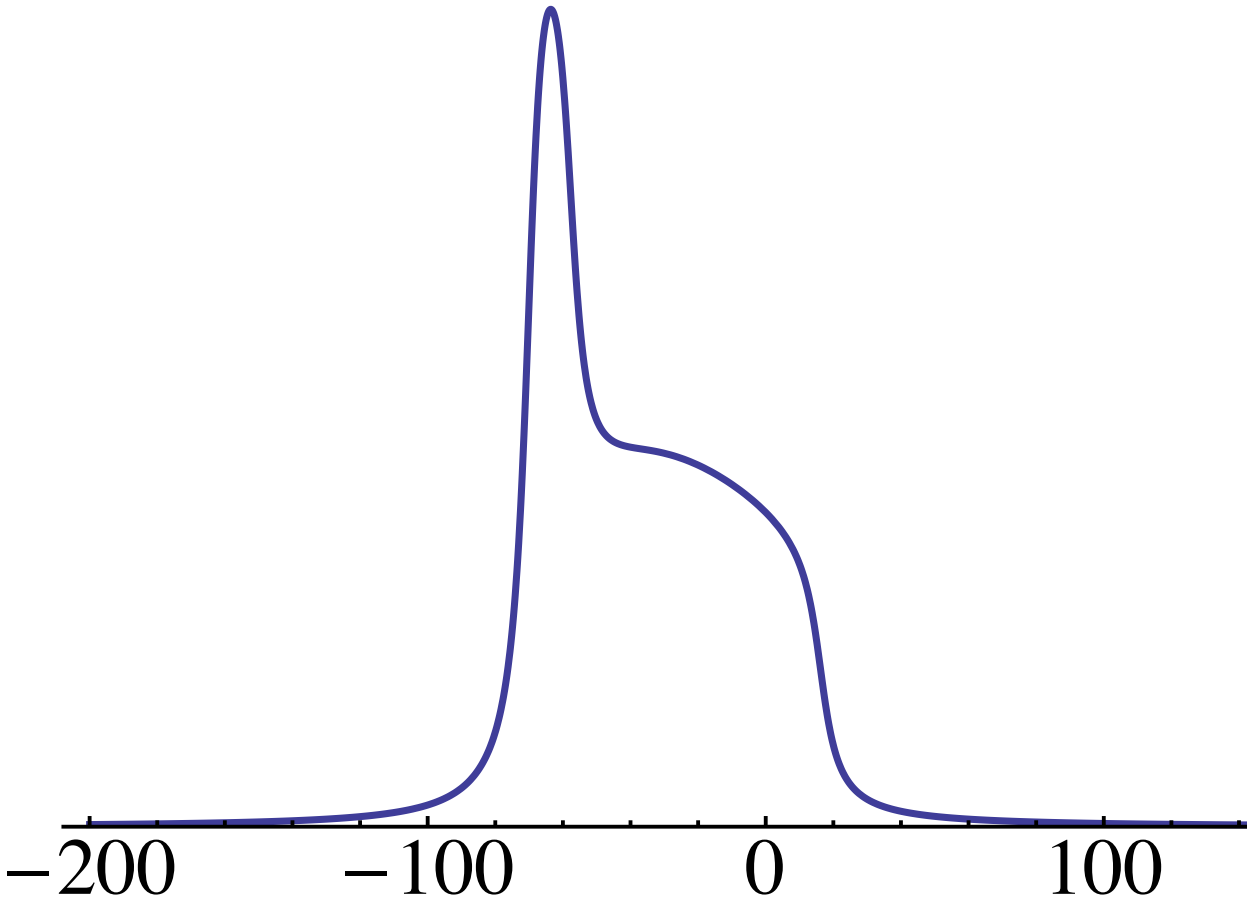
−200
−100
0
100

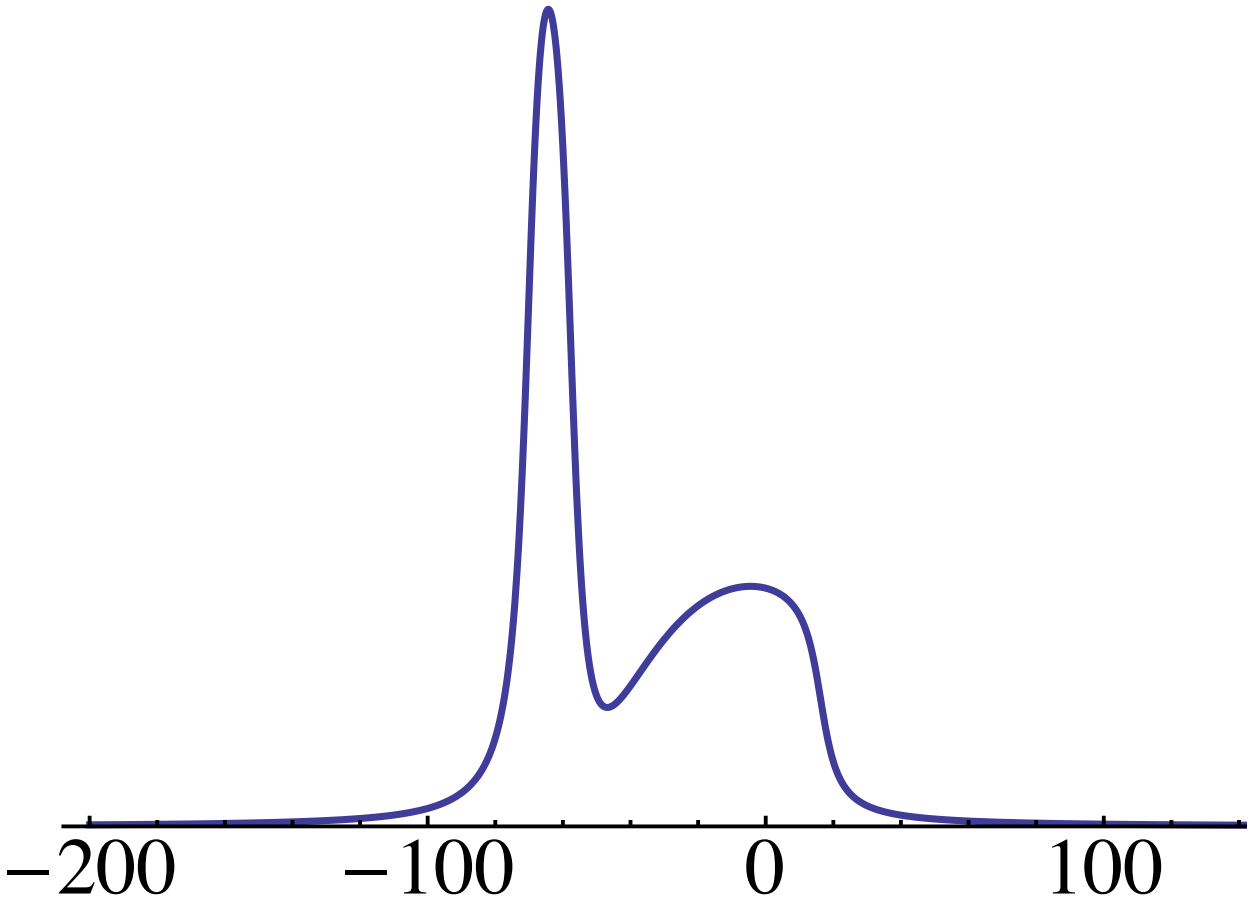
−200
−100
0
100

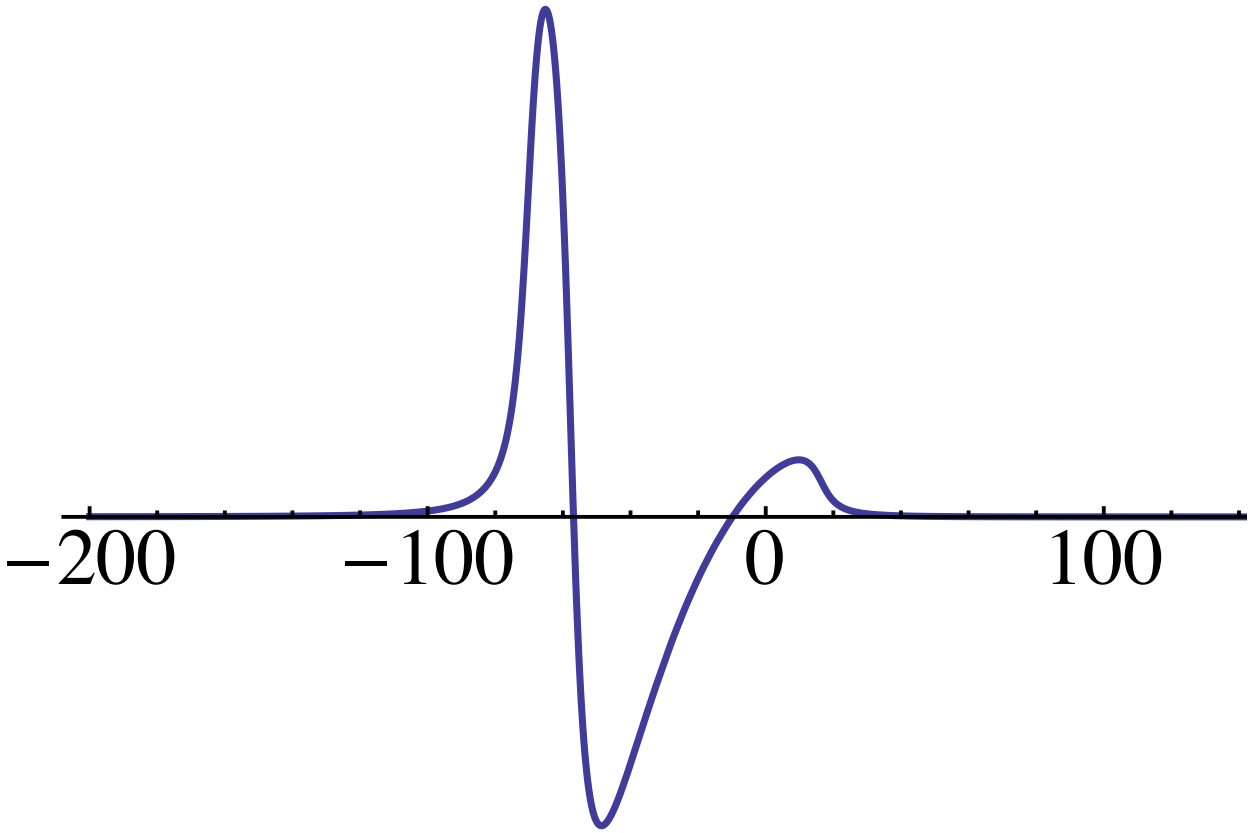
−200
−100
0
100

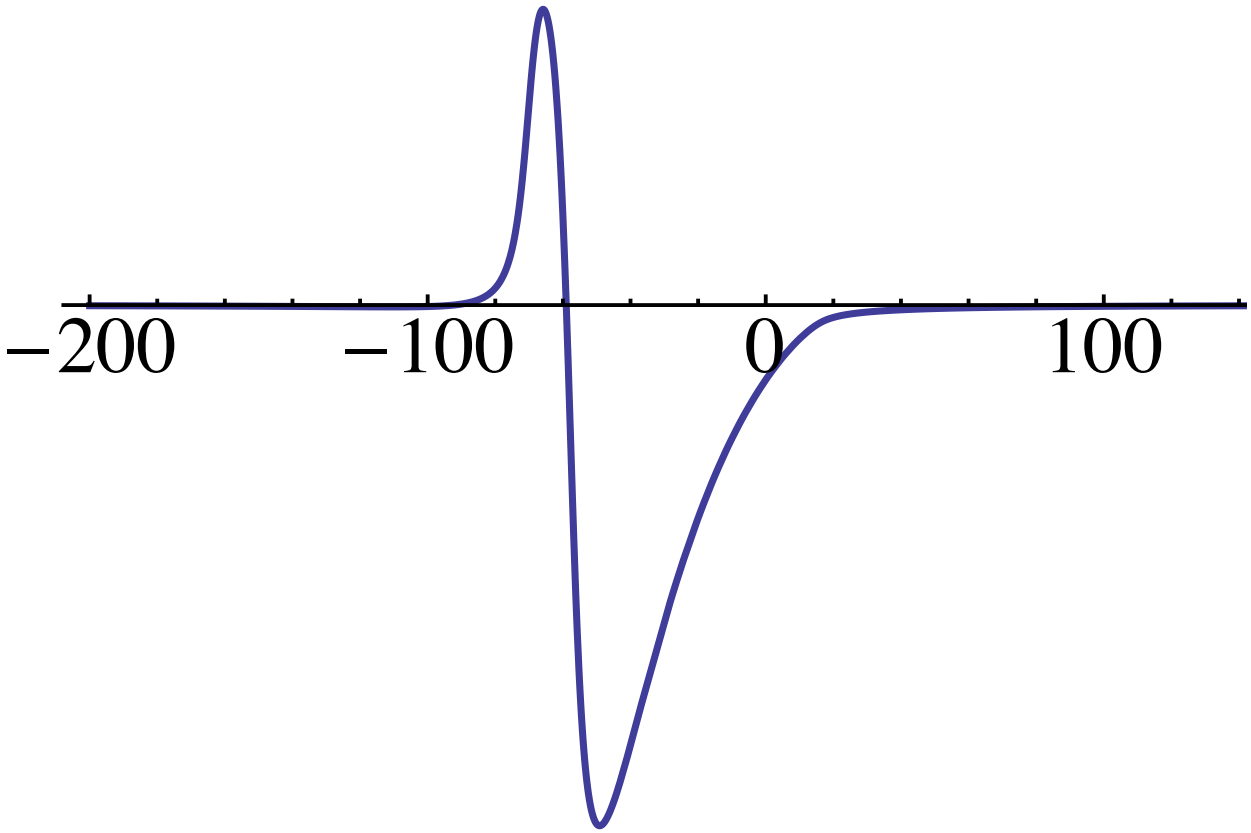
−200
−100
0
100

```
(*imagea[ν_]:=
 10^15*NIntegrate[Iz69[z,c/(855*10^-9)*h/(1.60217646*10^(-19)),19/(.25*.25*Pi)]/
    (1+((ν-z*grad*γ71/(2*Pi)/1000)/Δ)^2),{z,0,350*10^-6}];
imageb[ν_]:=10^15*NIntegrate[Iz69[z,c/(835*10^-9)*h/(1.60217646*10^(-19)),
     19/(.25*.25*Pi)]/(1+((ν-z*grad*γ71/(2*Pi)/1000)/Δ)^2),{z,0,350*10^-6}];
imagec[ν_]:=10^15*NIntegrate[Iz69[z,c/(830*10^-9)*h/(1.60217646*10^(-19)),
     19/(.25*.25*Pi)]/(1+((ν-z*grad*γ71/(2*Pi)/1000)/Δ)^2),{z,0,350*10^-6}];
imaged[ν_]:=10^15*NIntegrate[Iz69[z,c/(825*10^-9)*h/(1.60217646*10^(-19)),
     19/(.25*.25*Pi)]/(1+((ν-z*grad*γ71/(2*Pi)/1000)/Δ)^2),{z,0,350*10^-6}];
imagee[ν_]:=10^15*NIntegrate[Iz69[z,c/(820*10^-9)*h/(1.60217646*10^(-19)),
     19/(.25*.25*Pi)]/(1+((ν-z*grad*γ71/(2*Pi)/1000)/Δ)^2),{z,0,350*10^-6}];
imagef[ν_]:=10^15*NIntegrate[Iz69[z,c/(810*10^-9)*h/(1.60217646*10^(-19)),
     19/(.25*.25*Pi)]/(1+((ν-z*grad*γ71/(2*Pi)/1000)/Δ)^2),{z,0,350*10^-6}];
(*imageg[ν_]:=10^15*NIntegrate[Iz69[z,c/(795*10^-9)*h/(1.60217646*10^(-19)),0.968]/
    (1+((ν-z*grad*γ71/(2*Pi)/1000)/Δ)^2),{z,0,350*10^-6}];
imageh[ν_]:=10^15*NIntegrate[Iz69[z,c/(750*10^-9)*h/(1.60217646*10^(-19)),0.968]/
    (1+((ν-z*grad*γ71/(2*Pi)/1000)/Δ)^2),{z,0,350*10^-6}];*)

imageam[ν_]:=
 10^15*NIntegrate[Iz69m[z,c/(855*10^-9)*h/(1.60217646*10^(-19)),19/(.25*.25*Pi)]/
    (1+((ν-z*grad*γ71/(2*Pi)/1000)/Δ)^2),{z,0,350*10^-6}];
imagebm[ν_]:=10^15*NIntegrate[Iz69m[z,c/(835*10^-9)*h/(1.60217646*10^(-19)),
     19/(.25*.25*Pi)]/(1+((ν-z*grad*γ71/(2*Pi)/1000)/Δ)^2),{z,0,350*10^-6}];
imagecm[ν_]:=10^15*NIntegrate[Iz69m[z,c/(830*10^-9)*h/(1.60217646*10^(-19)),
     19/(.25*.25*Pi)]/(1+((ν-z*grad*γ71/(2*Pi)/1000)/Δ)^2),{z,0,350*10^-6}];
imagedm[ν_]:=10^15*NIntegrate[Iz69m[z,c/(825*10^-9)*h/(1.60217646*10^(-19)),
     19/(.25*.25*Pi)]/(1+((ν-z*grad*γ71/(2*Pi)/1000)/Δ)^2),{z,0,350*10^-6}];
imageem[ν_]:=10^15*NIntegrate[Iz69m[z,c/(820*10^-9)*h/(1.60217646*10^(-19)),
     19/(.25*.25*Pi)]/(1+((ν-z*grad*γ71/(2*Pi)/1000)/Δ)^2),{z,0,350*10^-6}];
imagefm[ν_]:=10^15*NIntegrate[Iz69m[z,c/(810*10^-9)*h/(1.60217646*10^(-19)),
     19/(.25*.25*Pi)]/(1+((ν-z*grad*γ71/(2*Pi)/1000)/Δ)^2),{z,0,350*10^-6}];
(*imagegm[ν_]:=10^15*NIntegrate[Iz69m[z,c/(795*10^-9)*h/(1.60217646*10^(-19)),0.968]/
    (1+((ν-z*grad*γ71/(2*Pi)/1000)/Δ)^2),{z,0,350*10^-6}];
imagehm[ν_]:=10^15*NIntegrate[Iz69m[z,c/(750*10^-9)*h/(1.60217646*10^(-19)),0.968]/
    (1+((ν-z*grad*γ71/(2*Pi)/1000)/Δ)^2),{z,0,350*10^-6}];*)

(*This series of plots simulates STRAFI data as a function of wavelength*)
(*Plot[{imagea[ν+70],imageam[ν+70]},{ν,-200,200}, PlotRange→All,Axes→{True,False},
  AxesStyle→Thick,TicksStyle→Thick,AxesLabel→{Style["  kHz",(FontSize→42),Bold,Black]},
  LabelStyle→(FontSize→42),PlotStyle→{Thickness[.005]}]
 Plot[{imageb[ν+70],imagebm[ν+70]},{ν,-200,200}, PlotRange→All,Axes→{True,False},
  AxesStyle→Thick,TicksStyle→Thick,AxesLabel→{Style["  kHz",(FontSize→42),Bold,Black]},
  LabelStyle→(FontSize→42),PlotStyle→{Thickness[.005]}]
 Plot[{imagec[ν+70],imagecm[ν+70]},{ν,-200,200}, PlotRange→All,Axes→{True,False},
  AxesStyle→Thick,TicksStyle→Thick,AxesLabel→{Style["  kHz",(FontSize→42),Bold,Black]},
  LabelStyle→(FontSize→42),PlotStyle→{Thickness[.005]}]
 Plot[{imaged[ν+70],imagedm[ν+70]},{ν,-200,200}, PlotRange→All,Axes→{True,False},
  AxesStyle→Thick,TicksStyle→Thick,AxesLabel→{Style["  kHz",(FontSize→42),Bold,Black]},
  LabelStyle→(FontSize→42),PlotStyle→{Thickness[.005]}]
 Plot[{imagee[ν+70],imageem[ν+70]},{ν,-200,200}, PlotRange→All,Axes→{True,False},
  AxesStyle→Thick,TicksStyle→Thick,AxesLabel→{Style["  kHz",(FontSize→42),Bold,Black]},
  LabelStyle→(FontSize→42),PlotStyle→{Thickness[.005]}]
 Plot[{imagef[ν+70],imagefm[ν+70]},{ν,-200,200}, PlotRange→All,Axes→{True,False},
  AxesStyle→Thick,TicksStyle→Thick,AxesLabel→{Style["  kHz",(FontSize→42),Bold,Black]},
  LabelStyle→(FontSize→42),PlotStyle→{Thickness[.005]}]
 (*Plot[{imageg[ν],imagegm[ν]},{ν,-200,200}, PlotRange→All,Axes→{True,False},
   AxesStyle→Thick,TicksStyle→Thick,AxesLabel→{Style["  kHz",(FontSize→42),Bold,Black]},
   LabelStyle→(FontSize→42),PlotStyle→{Thickness[.005]}]
  Plot[{imageh[ν],imagehm[ν]},{ν,-200,200}, PlotRange→All,Axes→{True,False},
   AxesStyle→Thick,TicksStyle→Thick,AxesLabel→{Style["  kHz",(FontSize→42),Bold,Black]},
   LabelStyle→(FontSize→42),PlotStyle→{Thickness[.005]}]*)
```

Appendix C

Modeling of Patterns of Nuclear Magnetization

Calculation of the Polarization Rate Ratio "f"

The ratio between the rates of the hyperfine and quadrupolar polarization mechanisms around a given defect is labelled "f":

$$f = \frac{T_Q}{T_H}. \tag{C.1}$$

In the high magnetic-field limit ($\omega_H \tau_H >> 1$) the hyperfine polarization rate is given by:

$$\frac{1}{T_H} = 2\Gamma\gamma_N^2 b_e^2(a_0)\frac{\tau_H}{\omega_H^2\tau_H^2}e^{4(1-\frac{r}{a_0})}. \tag{C.3}$$

The quadrupolar polarization rate is

$$\frac{1}{T_Q} = 2\Gamma(1-\Gamma)(\frac{|e|R_{14}Q}{12\hbar})^2(\frac{|e|}{4\pi\epsilon\epsilon_0})^2(\frac{K_1(\theta)\tau_Q}{\omega_N^2\tau_Q^2} + \frac{K_2(\theta)\tau_Q}{\omega_2^2\tau_Q^2})\frac{S^2(r)}{\frac{r^4}{a_0^4}}, \tag{C.4}$$

which in the high magnetic field limit ($\omega_N \tau_Q >> 1$) reduces to:

$$\frac{1}{T_Q} = 2\Gamma(1-\Gamma)(\frac{|e|R_{14}Q}{12\hbar})^2(\frac{|e|}{4\pi\epsilon\epsilon_0})^2(\frac{6}{\omega_N^2\tau_Q})\frac{S^2(r)}{\frac{r^4}{a_0^4}} \tag{C.5}$$

with

$$S(r) = 1 - (1 + \frac{2r}{a_0} + \frac{2r^2}{a_0^2})e^{\frac{-2r}{a_0}}. \tag{C.6}$$

Here ω_N is the frequency associated with a $\Delta I_z = 1$ nuclear spin transition and $\omega_2 \sim 2\omega_N$ is the frequency associated with a $\Delta I_z = 2$ transition. Using the high magnetic field limit for both polarization mechanisms, the ratio becomes

$$f = \frac{e^{\frac{-4r}{a_0}} r^4}{S^2(r)} \frac{\Gamma}{1-\Gamma} \frac{\gamma_N^4}{R_{14}^2 Q^2} \frac{768\sigma_e b_e^2(a_0) e^4 \epsilon^2 \epsilon_0^2 \hbar^2}{\sigma_c \gamma_e^2 |e|^4}. \tag{C.7}$$

Equilibrium and Steady State Polarizations

The quadrupolar polarization mechanism is driven by electron capture and recombination at recombination centers, thereby coupling the nuclear Zeeman energy reservoir to the electron kinetic energy reservoir. The electrons are assumed to thermalize rapidly, so that the electron kinetic temperature is equal to the lattice temperature. For a spin-$\frac{3}{2}$ system the polarization is given by

$$I_{Q,0} = \frac{1}{2} \tanh[B_0 \gamma_N \hbar/(2kT)] + \tanh[B_0 \gamma_N \hbar/(kT)]. \tag{C.8}$$

At 6 K for ^{71}Ga in a field of 9.4 T, this corresponds to a polarization of approximately 0.1% or $\sim$ 56 Gauss[43]. The steady-state value for a spin-$\frac{3}{2}$ nucleus undergoing DNP induced by a contact hyperfine interaction is

$$I_{H,0} = 5\Delta S_z \tag{C.9}$$

where ΔS_z is the departure of S_z from its thermal equilibrium value. This parameter is given by

$$\Delta S_z = \frac{S_0 - S_{eq}}{1 + \frac{\tau}{T_{1e}}} \tag{C.10}$$

where S_0 is the polarization of electrons due to excitation selection rules, S_{eq} is the thermal equilibrium polarization of electrons, and τ and T_{1e} respectively denote the electron recombination lifetime and spin-lattice relaxation time of electrons. Hyperfine-induced nuclear polarization in semiconductors has been measured to be of the order of 10%[40]. 10% polarization in GaAs corresponds to a nuclear field of approximately 5600 Gauss[43].